Solar Energy Materials & Solar Cells 258 (2023) 112407

Contents lists available at ScienceDirect

Solar Energy Materials and Solar Cells

journal homepage: www.elsevier.com/locate/solmat

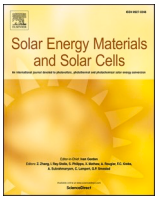

Moisture induced degradation in field-aged multicrystalline silicon photovoltaic modules

Oscar Kwame Segbefia *, Naureen Akhtar, Tor Oskar Sætre

Department of Engineering Sciences, University of Agder, 4879, Grimstad, Norway

ARTICLE INFO

Keywords:
Moisture ingress
Lead oxide
Metal stannate
Silver acetate
Metal-ligand
Photosensitive

ABSTRACT

Moisture ingress is one of the key fault mechanisms responsible for photovoltaic (PV) devices degradation. Understanding moisture induced degradation (MID) mechanisms in field-aged PV modules is more reflective of the reality in the field. In the present work, MID products of reclaimed solar cells from 20-year-old field-aged silicon PV modules is investigated. The defective areas in the PV modules were identified using visual inspection, electroluminescence (EL), ultraviolet fluorescence (UV–F), and infrared thermal (IR-T) techniques. SEM-EDS analysis is used to elucidate the role of moisture on the observed degradation mechanisms. Degradation of the ethylene vinyl acetate (EVA) encapsulation produces acetic acid, carbon dioxide, phosphorus, sulfur, fluorine, and chlorine. Migration of metal ions under the influence of moisture ingress makes the formation of oxides, hydroxides, sulfides, phosphates, acetates, and carbonates of silver, lead, tin, copper, zinc, and aluminum feasible. Also, other competing reactions can lead to the formation of stannates of copper, silver, sodium, and zinc. Another observation is that, in the presence of MID species, Pb is preferentially corroded (to form lead acetate complexes) instead of the expected sacrificial Sn in the solder. These MID species account for different defects and fault modes that lead to parasitic resistance losses. This is witnessed by the 1.2%/year degradation in the P_{max} of the PV module.

1. Introduction

Moisture ingress is one of the key routes to photovoltaic (PV) devices degradation [1–5]. In the field, and under environmental stressors (e.g., high temperature, humidity, ultraviolet radiation), moisture can enter the PV modules from the edges, 'breathable' backsheets, and via cracks or voids [3,4,6]. These channels of diffusion for moisture (water, oxygen, and carbon oxides), are created during manufacturing, transportation, handling, and installation [4,7–9]. Long periods of heavy snow and wind loads complicate the situation in the Nordics. In the Nordics, the global annual average climate moisture index (CMI) is greater than 0.5 [5]. CMI is the measure of moisture availability at a specific place and time based on the precipitation and moisture absorption of the local atmosphere [10]. Hence, the CMI can be an indicator of the degree of moisture susceptibility of electronic devices (including solar panels) in a particular place.

There are efforts within the PV community as regards preventing, detecting, and mitigating moisture ingress and its effects in PV modules. The use of encapsulation materials with high adhesion and moisture barrier qualities, desiccant stacked sealants, and imbedded moisture sensors are some of the ways of achieving this objective [4,11]. In hermetic PV module configurations (e.g., double glass PV modules), moisture ingress into the modules is limited. However, the escape of moisture induced degradation (MID) or corrosion species is also limited. This can therefore lead to accelerated degradation of field deployed solar panels. A comprehensive review on moisture ingress in crystalline silicon PV modules has been provided by Segbefia et al. [4]. In the field, PV modules are exposed to multiple environmental stressors such as high humidity, temperature, UV radiation, and soiling during their operation in the field. The role of these environmental stressors in the formation of MID species and subsequent degradation processes in the PV module is significant and is the reality in the field. However, in the absence of moisture ingress (under humidity exposure), formation of MID species is impossible, irrespective of the environmental stressors the PV module is exposed to. Hence, understanding the mechanisms and effects of MID in field-aged solar PV modules is the best way to understand what happens in the field.

Once moisture enters the PV module bulk, electrochemical reactions

* Corresponding author. Department of Engineering Sciences, University of Agder, 4879, Grimstad, Norway.
E-mail address: oscar.k.segbefia@uia.no (O.K. Segbefia).

https://doi.org/10.1016/j.solmat.2023.112407
Received 2 March 2023; Received in revised form 16 May 2023; Accepted 30 May 2023
Available online 11 June 2023

are initiated. The ethylene vinyl acetate (EVA) encapsulation when exposed to moisture and light, can produce acetic acid [4,8,12]. In the presence of excess moisture and light, the acetic acid can breakdown to formic acid, and the incidence of corrosion is more likely [4]. Moisture and acetic acid can attack the metal grids to form their respective metal oxides, acetates, hydroxides, and bicarbonates [13–17]. The copper ribbon, lead, and zinc (from the silver paste) can also degrade into copper (Cu), lead (Pb), and zinc (Zn) acetates, respectively in the presence of acetic acid and moisture [14,16,18]. Recently, Jeffries et al. [14] reported silver acetate as the main product of acetic acid corrosion in PV modules. Moreover, it was reported that the corrosion of intermetallic compounds (IMC) in acetic acid depend on the concentration of Ag in the paste [14]. These degradation products can also lead to the degradation of the solar cells, corrosion, and optical degradation [12–19].

In the presence of moisture, aluminum (Al) and sodium (Na) ions can also leach from the Al- frame and the front glass, respectively into emitter regions in the solar cells and modules, hence, cause potential induced degradation (PID) [20,21]. These MID processes can also lead to the incidence of microcracks and/or snail trails, optical degradation, and antireflection coating (ARC) degradation, among others [8,22–24]. These degradation mechanisms affect the efficiency and performance reliability of PV plants [25,26]. For instance, silver oxides deposited on the metal grids lead to increased series resistance [14,17,18,27]. Degradation of the encapsulation and the silver grids in the presence of moisture can lead to the formation of silver carbonates, sulfides and phosphates which are precursors for snail trails [13]. The silver carbonate can reflect, absorb, and scatter light photons [28]. This influences the charge carrier generation, transport, and recombination in the module bulk. Resistance effects leads to localized hotspots and increased module temperature, and hence, a drop in the power output [29]. MID products such as lead, silver, copper oxides, acetates, and carbonates appear as dark spots in electroluminescence (EL) and ultraviolet fluorescence (UV–F) images, and in infrared thermal (IR-T) images, they are seen as hotspots [12,14,17,19,30].

Electroluminescence, photoluminescence (PL), infrared thermal, ultraviolet fluorescence, dark lock-in thermography (DLIT), current-voltage (I–V), and visual inspection techniques have been used to detect these defects and fault mechanisms in PV plants [4,12,17]. The collective advantage of these techniques is that they are non-destructive. However, these techniques are incapable of establishing the microstructural causes of the observed degradation mechanisms. Hence, investigations to unravel the root causes of these degradation mechanisms (based on degradation products) employ microscopic and spectroscopic methods. MID species can be detected using scanning electron microscopy (SEM), energy dispersive spectroscopy (EDS), electron beam induced current (EBIC), fourier transform infrared (FTIR) spectroscopy, X-ray photoelectron spectroscopy (XPS), atomic force microscopy (AFM), thermo-gravimetric analysis (TGA), Raman spectroscopy, etc. [4,8,12,31]. Even though these techniques are destructive, they are well established. The prospects of employing both the destructive and non-destructive methods to detect MID mechanisms have been reported [8,12,16,17,28,32]. In these investigations, efforts were made to understand the MID observed in non-destructive methods at the microstructural level. Indeed, this twin approach employs the strengths of both methods for defects and fault diagnosis.

Most recently, the present authors reported the effect of moisture on the morphological degradation of titania antireflection coatings (ARCs) [33]. The influence of the degradation of these coatings on the efficiency of the PV module is important. With emerging PV applications such as floating PV and agro-PV at sight, understanding the mechanisms and effects of MID in PV modules under multiple real field environmental stressors is more important than ever. Up to now, research on the microstructural signatures of MID in PV modules appear to focus more on the EVA encapsulation, silver grids, solder, and copper ribbons [8, 12–19,32,34]. Most investigations ignore the effect of moisture ingress on the solar cell microstructure itself and its degradation mechanisms. In addition, only a few of these reports were carried out on field-aged PV modules [12,13,15,32,34]. Moreover, we have not come across any published work on the effects of MID on silicon solar cells. Additionally, none of the reports on the effect of MID on solar PV modules was done in the Nordics, where the effect of moisture ingress is a huge challenge, due to the high CMI in this climate. Hence, a holistic investigation on all the solar cell components: solar cell, silver grids, solder, and copper ribbons in the Nordic is necessary. The effect of moisture ingress on the degradation of the EVA encapsulation is not presented in this work, as it is the subject of another investigation.

In the present work, the MID of reclaimed solar cells from a 20-year-old field-aged multicrystalline silicon (mc-Si) PV module is investigated. The electrical characteristics of the PV module were acquired via I–V characterization. The defective areas in the PV modules were identified using visual inspection, EL, IR-T, and UV-F techniques. The microstructural characterization of the reclaimed solar cells employed SEM-EDS techniques. A brief description of the PV modules and the methods used for the investigation are given in Section 2, followed by the findings and the discussions in Section 3.

2. Material and methods

The field-aged NESTE NP100G12 PV Module X for this investigation was chosen from a batch of PV modules which were installed on a Renewable Energy Park in Dømmesmoen, Grimstad (58.3447° N, 8.5949° E), Norway in the year 2000. However, the PV modules on the Energy Park were decommissioned in 2011 and were kept securely for research purposes. The manufacture's data sheet and the measured average electrical data of the 43 field-aged PV modules and the PV module selected for this study is summarized in Table 1. Details of the Energy Park and the catalogue of the defects and failure modes of these PV modules was reported earlier [5].

The module comprises of a (0.1 × 0.1) m^2 mc-Si solar cells with screen printed aluminum (Al-) grids at the back and titania (TiO_2) ARC. The cell is sandwiched between ethylene vinyl acetate (EVA) encapsulant. The front glass and the backsheets were made from a low iron tempered glass and white multi-layered Tedlar®/Polyester/Tedlar® (TPT), respectively. The rest of the module's components are 2 junction boxes, each containing a bypass diode and an anodized Al- frame. Tinned copper was used for the interconnect ribbons. The panel is made up of 72 cells connected serially in 3 parallel substrings [21]. The suspected areas were extracted using a water jet cutting technique, followed by subsequent solvent treatment. The reclaimed solar cell samples (from the defective areas) were then taken through SEM-EDS analyses. The experimental procedure for the study is illustrated in Fig. 1. Table 1 suggests that, after 20 years, the electrical characteristics of PV Module X is similar to the average electrical characteristics of the 43 field-aged PV modules. Hence, the degradation mechanisms in these field-aged PV modules might be identical.

2.1. Visual inspection

A comprehensive visual inspection on the solar PV panel was

Table 1
The manufacturer's data sheet and the measured average electrical parameters of the 43 solar PV modules and PV Module X in 2020 normalized to Standard Test Conditions (STC).

Year	P_{max} (W)	V_{oc} (V)	V_{mpp} (V)	I_{mpp} (A)	I_{sc} (A)	FF (%)	η (%)
2000 (Data sheet)	100	21.6	16.7	6.0	6.7	70	13
2020 (43 modules)	78.2	19.7	14.7	5.3	6.0	66	10
2020 (Module *X*)	76.0	19.8	14.4	5.3	6.0	64	10

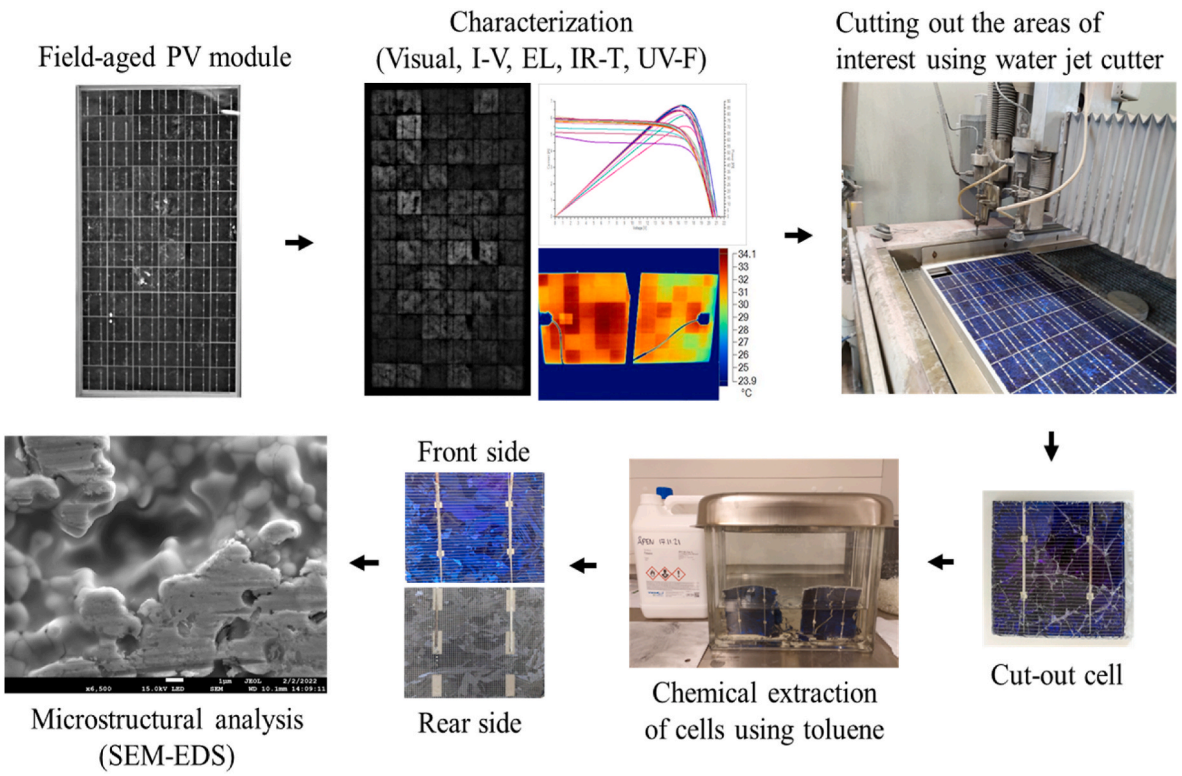

Fig. 1. Experimental procedure for the microstructural investigation of the moisture induced degradation products in the field-aged PV module.

conducted under clear sky outdoor conditions. We also acquired high-resolution photographs from the panel: front and rear sides in a dark room with optimized light exposure. This extra step was invaluable in identifying defects which were hidden in the conventional visual inspection method. The IEC 61215: 2016 standard was adhered to in collecting and reporting the data from the visual inspection of the solar panel.

2.2. I–V measurements

Information on the electrical parameters was acquired from the solar panel using a handheld I–V 500w I–V Curve Tracer as per the IEC 60904-1 standard. The measurements were done under Standard Test Conditions (STC) and data on the maximum power (P_{max}), short circuit current (I_{sc}), open circuit voltage (V_{oc}), fill factor (FF), maximum power point voltage (V_{mpp}), maximum power point current (I_{mpp}), module temperature (T_m), and in-plane irradiance (G_I) characteristics of the panel was documented. STC specifies cell temperature (25 °C), an in-plane irradiance (1000 W/m^2) and air mass 1.5 (AM1. 5) spectrum for commercial PV panels. The experiments were performed under clear sky in-plane irradiance (960–1040 W/m^2) and wind speed (<2 ms^{-1}) conditions. The I–V Tracer converted data points to STC automatically to minimize errors related to data recording and processing. The temperature coefficient (β_x) of each electrical parameter (x) was computed using regression plots: a graph of T_m versus electrical parameter, x. Details of the temperature coefficient measurement was presented earlier [21,35].

2.3. Ultraviolet fluorescence (UV–F) imaging

UV-F imaging is a handy tool for detecting cracks and moisture induced degradation (e.g., cell and optical degradation) in PV plants [36,37]. In the presence of ingressed moisture (e.g., water and oxygen), fluorescent degraded species (in the solar panel's encapsulation) undergo photochemical transformations into nonfluorescent species [37]. Under UV light, degraded areas show darker traces due to defects photoquenching. This helps to differentiate defective areas from healthy areas in the solar PV panel [36]. UV-F images of PV module X was acquired in a dark room using a TROTEC® LED UV TorchLight 15F ($\lambda \approx$ 365 nm) equipped with a Wolf eyes FD45 spectrum filter. The experiments were done as per the International Energy Agency (IEA) recommended procedure [25,38].

2.4. Electroluminescence (EL) imaging

EL imaging is a suitable tool for quantifying resistive losses in old PV modules affected by cracks and severed metal grids. EL characteristics of the solar panel was acquired in a dark room using the BrightSpot EL Test Kit: a 24 megapixels modified DSLR (digital single-lens reflex) Nikon D5600 camera, a DC power supply device set, and a laptop computer equipped with data acquisition and processing software. The measurements were done as per the IEC 60904- 13 standard and the IEA prescribed method [26]. The EL characterization was performed under I_{sc} and 0.1I_{sc} forward bias conditions in a dark room as reported earlier [5,21].

2.5. Infrared thermal (IR-T) imaging

The field-aged PV module was taken through IR-T measurements using the Fluke Ti400 Infrared Camera ($\lambda \approx$ 650–1400 nm) as per the IEA prescribed procedure [26] and the IEC 62446- 3 standard. Details of the experimental set up for the outdoor investigation under clear sky outdoor conditions at the Rooftop facility was reported earlier [21]. For these measurements, the IR thermal images were acquired after soaking the solar panel in the sun for at least 15 min.

2.6. Solar cell reclamation and microstructural analysis

The regions of interest (areas affected by microcracks and moisture ingress) were extracted using a Water Jet NC 3060D Beveljet cutting machine. The machine which is controlled by a CNC software employs a

fine water jet with abrasive under ultra-high pressure (ca. 4000 bar) for sample cutting. The technique is very suitable when low cutting temperature is desired. The as cut samples (consisting of the front glass, encapsulant, copper ribbons, solar cell, and backsheet) was separated using toluene. The samples were immersed in the toluene at room temperature for 14 days, refer to Fig. 1. After 7 days, the front glass and front encapsulant were separated. However, the backsheet could be removed after 14 days. The extracted solar cells from the field-aged PV module were analyzed using a field emission scanning electron microscope (SEM) (JEOL 7200F) equipped with an energy dispersive X-ray spectrometer (Octane Elect EDS system from EDAX®-AMETEK®) to identify the MID products. The components of the solar cell extracted from the field-aged PV module that were investigated are shown in Fig. 2.

The copper busbars, located around the perimeter of the PV module, connect the Cu interconnect ribbons. They collect and deliver cumulative current to the junction boxes. The silver fingers are perpendicular to the Cu ribbons whilst the Ag busbars lie beneath the Cu ribbons. The Cu ribbons are connected to the solar cells and the Ag grids with the solder, which is made up of lead and tin. The effect of moisture ingress is more severe around the perimeter of PV modules [12,30]. Hence, the solar cells and other components for the SEM-EDS investigation were extracted from the edge of the field-aged PV module.

3. Results and discussion

3.1. Visual inspection

Fig. 3 shows some of the results from the visual inspection of the PV module. Fig. 3a shows the photographic images of a pair of solar cells acquired under clear sky outdoor conditions highlighting signs of optical degradation e.g., delamination and discolouration of the encapsulation. Fig. 3b and c are images acquired from the same area of the field-aged PV module under clear sky outdoor and dark room conditions, respectively. Fig. 3b and c shows complementary signs of MID degradations, which could not be seen in either of these Figs. alone.

Moisture induced discoloration is shown in the upper left corner in Fig. 3b whilst Fig. 3c shows accumulation of MID species around the solder joint. Fig. 3d and e shows the inner side of the TPT backsheets of solar cells extracted from the middle and the edge of the field-aged PV Module X, respectively. Fig. 3d is not discolored whereas Fig. 3e is discolored. Discoloration of the backsheets is a typical sign of degradation due to UV radiation. Yet, the effect of UV radiation is expected to be uniform across the backsheet in the same PV module. Hence, we believe that the degradation of the EVA encapsulation and the TPT backsheets of the PV module is due to moisture ingress. In Section 3.6, SEM-EDS analyses will be used to support this observation. Dark discolored backsheets were also observed in optically degraded PV modules

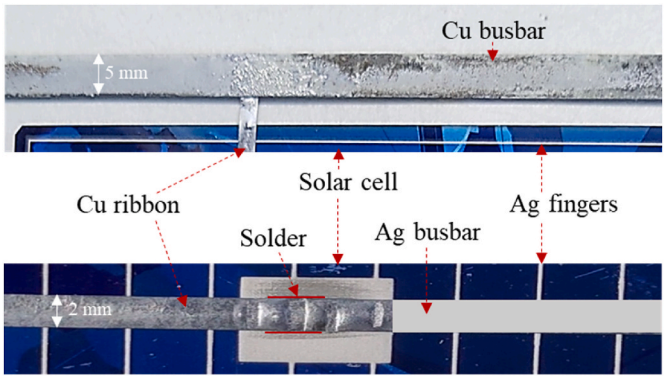

Fig. 2. Components of the field-aged PV module extracted for the SEM-EDS analysis.

by other researchers [39]. Fig. 4 shows the visual images acquired from the same area of a solar cell close to the edge of field-aged PV Module X showing the degradation state of a Cu ribbon. Fig. 4a was acquired under clear sky outdoor conditions and Fig. 4b was acquired under optimized dark room conditions. The figure shows corrosion and oxidation of the metal grids, and trapped moisture and MID species, especially around the solder joint. Corrosion of metal grids around the solder joint area due to moisture ingress was also reported by other authors [17–19,23]. Fig. 4 suggests that Module X has been affected by moisture induced defects.

Corrosion at the solder joint is attributed to the dissolution of lead and tin (main components of solder) in moisture and acetic acid due to galvanic corrosion [17]. This could be due to low adhesion at the solder joint or the presence of defects during the soldering process [18]. The observed corrosion at the solder joint region could also be as a result of MID of the Ag grids [8]. However, this corrosion mechanism is only feasible in the presence of moisture. It can be seen in Fig. 4 that the metal grids have been masked out by MID species. The optical integrity of these areas in Fig. 4 appears to be compromised as well. Earlier investigation by the present authors established that more than 90% of these field-aged PV modules were affected by optical degradation, though other stressors such as UV radiation also can play significant roles [5,40]. This observation agrees with other reports on the role of MID products in optical degradation of PV modules [13,14,16,27].

3.2. I–V characteristics of the field-aged PV module

Fig. 5 shows the electrical characteristics of field-aged PV Module X. Degradation in the P_{max}, V_{oc}, and I_{sc} due to increased series resistance (R_S), low shunt resistance (R_{SH}), and reduced fill factor are illustrated. The annual degradation in P_{max}, V_{oc}, and I_{sc} for PV Module X were found to be approximately 1.2%, 0.4%, and 0.5%, respectively. The degradation in PV Module X is similar to the average degradation in all the field-aged PV modules. Corrosion of metal grids, optical degradation, and PID due to moisture ingress are known to be the underlying causes of resistance losses, hence, power degradation [4,25]. Considering the location of the present investigation, the influence of MID mechanisms on the degradation of these PV modules is high [5]. MID products such as acetic acid, acetates, oxides and hydroxides of silver, lead, silver, tin, and copper were reported to be responsible for increased series resistance and shunting [12,14,30].

It was reported that increased series resistance, shunting, and ARC degradation are the three key fault mechanisms that lead to power degradation [8,22]. The effect of moisture ingress on the degradation of the ARC in PV Module X was reported earlier [33]. On the other hand, increased series and decreased shunt resistances due to a variety of defects and fault modes lead to increased module operating temperature (T_m) [29,40]. The temperature coefficients of the PV module can therefore be an indicator of the effect of resistance losses [29,41,42]. Table 2 summarizes the average relative temperature coefficients of PV Module X. The average temperature coefficient of efficiency ($\beta_{\eta m}$) of the field-aged PV module was found to be approximately −0.5%/°C, which is equivalent to the average $\beta_{\eta m}$ of all the field-aged PV modules [5].

$\beta_{\eta m}$ is the cumulative contributions from the temperature coefficients of V_{oc} (β_{Voc}), I_{sc} (β_{Jsc}), fill factor (β_{FF}), V_{mpp} (β_{Vmpp}), and I_{mpp} (β_{Jmpp}). The β_{Jsc} among other factors, depends strongly on the collection fraction (f_c) [29,43]. The f_c is the fraction of photogenerated charge carriers within the solar cell that could be extracted from the solar cell as photocurrent [44]. Hence, the f_c depends on the resistive losses due to optical degradation and parasitic absorption within the solar cell [29].

From Table 2, the β_{Jsc} for PV Module X is relatively low, indicating increased resistance losses. The β_{Jsc} from other reports were higher, with $\beta_{Jsc} > 0.06$ [42,45]. The observed lower β_{Jsc} for the field-aged PV module suggests degradation due to reduced f_c [29]. Strikingly, the β_{Jmpp} is negative as reported earlier by Segbefia and Sætre [21] for field-aged PV modules affected by PID. Migration of cations e.g., Na ions to the emitter regions of solar cells are responsible for PID [9]. Moisture ingress has

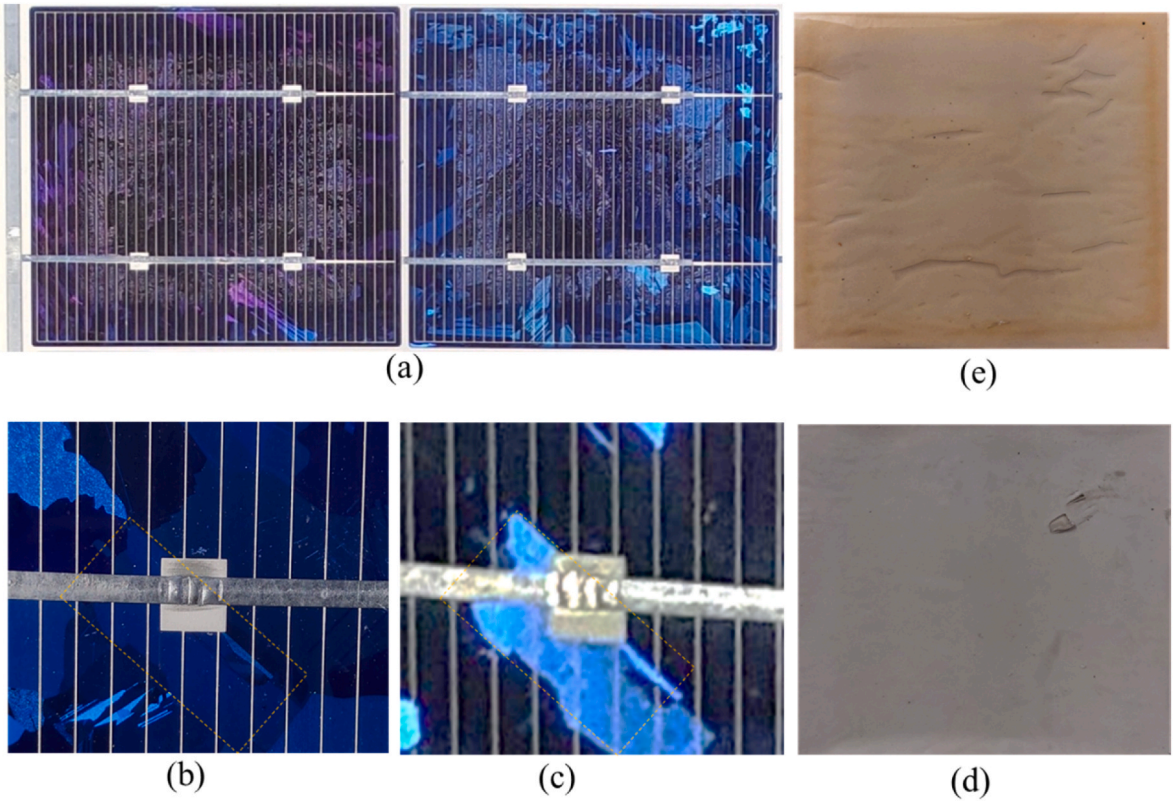

Fig. 3. Visual images of the field-aged PV module. Photographic images of a (a) pair of solar cells showing signs of delamination and discolouration of encapsulation, a copper ribbon under (b) clear sky outdoor and (c) optimized light exposure in dark room conditions, and the inner side of the backsheet of a solar cell (d) not affected and (e) affected by moisture ingress.

Fig. 4. Part of a solar cell and degraded copper ribbon showing signs of moisture ingress. Images were acquired under (a) clear sky outdoor and (b) optimized light exposure dark room conditions from the same area of the solar cell.

been reported for the migration of these ions to sensitive areas such as the emitter of solar cells [46]. Hence, it is likely that PV Module X is suffering from PID as well due to moisture ingress, as will be demonstrated with the EL, IR-T, and SEM-EDS characteristics.

3.3. Electroluminescence (EL) characteristics

Fig. 6 shows the EL and UV-F images of field-aged PV Module X. Fig. 6a and b are the EL images acquired under I_{sc} and $0.1I_{sc}$ forward bias conditions, respectively. Fig. 6a shows the presence of microcracks and darker regions at the edges of the solar cells. Microcracks are conduits and reservoir for moisture ingress [4]. Darker marks at the edges of the solar cells suggest that degradation at the cell edges is more severe [26]. From Fig. 6b, it can be seen that the majority of the solar cells around the edge of the module are darker than those in the middle of the module. Dark cell patterns (especially around the edge of the module) indicate the presence of MID products such as metal oxides and acetates [12,14,19,30]. In addition, most of the darker cells are located nearer to the perimeter of the PV module. Degraded cells around the edges of the PV module indicate moisture induced PID, as indicated by the β_{Jmpp}. This observation is in line with other reports [25,26]. The satellite cells in the areas affected by cracks also show darker patterns.

3.4. Ultraviolet fluorescence (UV–F) characteristics

PV Module X shows weak fluorescence and luminescence signals, which align with earlier investigations by the present authors [35,40]. The majority of the batch of field-aged PV modules from which PV

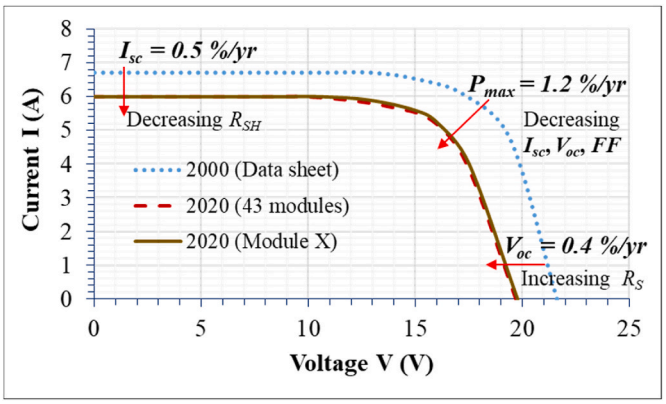

Fig. 5. Electrical characteristics of the solar PV module. Degradation per year (yr) in P_{max}, V_{oc}, and I_{sc} as well as the effect of the series resistance (R_S), shunt resistance (R_{SH}), and fill factor (FF) are illustrated.

Table 2
Average relative temperature coefficients of solar PV Module X.

Temperature coefficient (%/°C)					
β_{Voc}	β_{Jsc}	β_{FF}	$\beta_{\eta m}$	β_{Vmpp}	β_{Jmpp}
−0.4	0.05	−0.2	−0.5	−0.5	−0.07

Module X was chosen were found to show weak fluorescence and luminescence signal intensities [5]. Fig. 6c, d, and 6e are the UV-F images of the corresponding marked out areas in Fig. 6a showing the evidence of microcracks and MID. Although most of the defective areas (microcracks) in the UV-F images correspond with the observation in the EL image (Fig. 6a), some microcracks were hidden in the EL images. Defects that do not affect current flow are not seen in EL images [26,47]. On the other hand, only degraded encapsulation areas are seen as dark areas in UV-F images [36,37].

Usually, these microcracks are located around the perimeter of the PV module. One reason for this observation is that, during manufacturing, handling and transportation of PV modules, the likelihood for microcracks formation is high. The thermal processing steps especially induces thermochemical stress, and hence, microcracking in the solar cells. Usually, some of the microcracks formed during the manufacturing phase of the production process are not detected. So, in the field, environmental and climatic stressors can make these microcracks degrade further, even into macrocracks. Very high and low ambient temperatures can induce microcracks in solar cells due to thermochemical stress. In addition, in environments with high humidity conditions, moisture can enter the PV module. Moisture ingress is more feasible where there are microcracks and other voids around the edges of the PV module. Moisture ingress can also initiate new microcracks or make existing microcracks degrade further [48].

Formation and degradation of microcracks under the influence of moisture ingress is one possible reason for the observed microcracks in

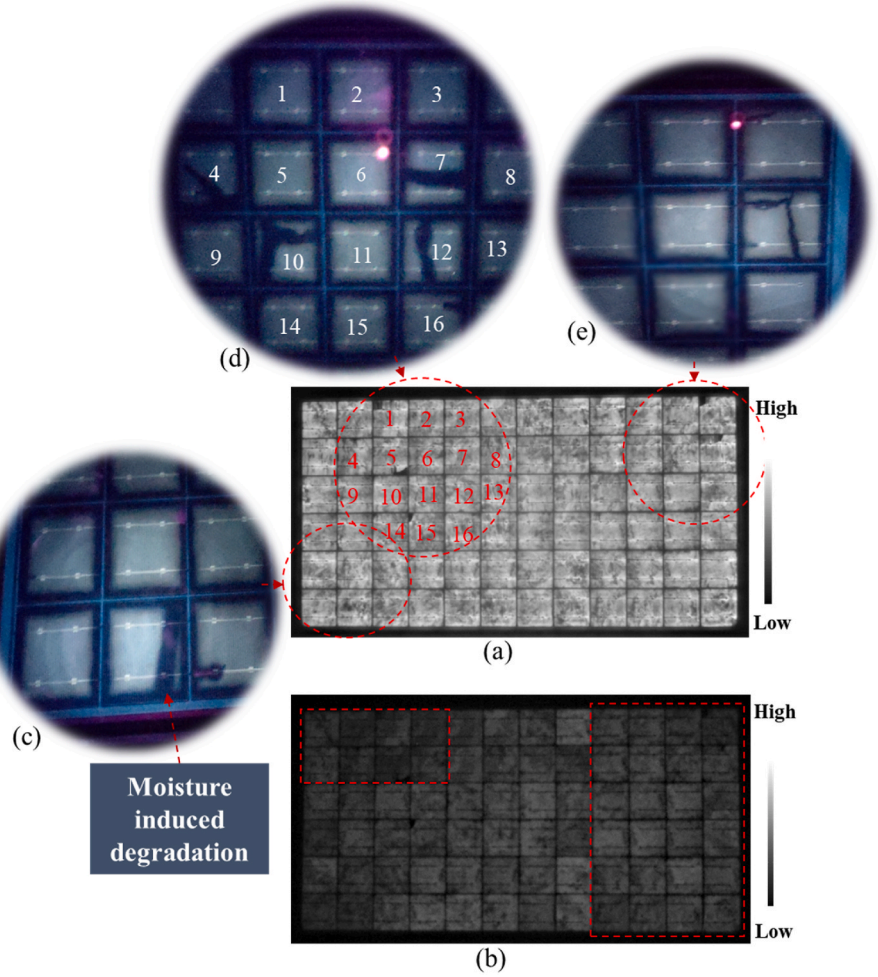

Fig. 6. EL characteristics of PV Module X acquired under (a) I_{sc} and (b) $0.1I_{sc}$ forward bias conditions. (c)–(e) UV-F characteristics of various parts of PV Module X showing signs of microcracks and MID. All images were acquired in a dark room.

Fig. 6c, d, and 6e. Specifically, the geometry of the microcracks and the presence of some of the microcracks was not very clear in the EL images. In Fig. 6c, the copper ribbon in the defective area appears unbroken. Hence, the position of the defect in Fig. 6c is not very clear in the EL images (Fig. 6a and b). This defect is likely a moisture induced degradation. In Fig. 6d, the copper ribbons of the defective cells (e.g., Cells 4, 7, 10 and 12) appear to be completely broken. These microcracks are also multidimensional to the busbars and are more critical to power loss. Since these microcracks are located close to the edge of the PV module, the influence of moisture ingress on the microcracks formation and degradation cannot be ruled out. The geometry and positions of the microcracks in Cells 4, 7, 10, and 12 are not very clear in Fig. 6a, however. Hence, UV-F technique is better suited for detecting moisture induced defects and fault modes.

In addition, the nature of the microcracks (e.g., crack width) in Fig. 6c and d shows further degradation of the microcrack regions which might be due to the influence of moisture ingress under multiple real field environmental stressors. The microcrack patterns in Fig. 6c and d are broader in width and extend beyond the immediate crack regions. However, the microcrack in Fig. 6e is narrower and suggests that the effect of moisture ingress on this crack region is less severe. In Fig. 6e, even though the microcrack is located at edge of the PV module, the microcrack appears to be opened inwards away from the Al- frame. However, in Fig. 6c, the microcrack opens towards the Al- frame. In Fig. 6c, the influence of moisture ingress from the edge of the module is greater than in Fig. 6e. In an earlier investigation on these field-aged PV modules, PV modules with strong fluorescence and luminescence signals show sharper crack patterns [40]. The effect of moisture on the degradation of microcracks was also observed elsewhere [48]. Moisture ingress induce the formation of silver and lead acetates, oxides, sulfides, and phosphates in the affected areas in PV modules [13,28]. These degradation products are witnessed as dark areas in EL and UV-F images [13,14,16].

3.5. Infrared thermal (IR-T) characteristics

Defective cells cause mismatch losses, hence, lead to inhomogeneous distribution of cell temperature (T_c) throughout the PV module. Defective cells operate at higher T_c and become hotspots. This in turn influences the T_m of the PV module. The difference in the T_c (ΔT) of the cell with the highest and lowest T_c can be an indication of the presence of specific defects and fault mechanisms [26,47,49]. Fig. 7a shows the IR-T image of PV Module X. The respective zoomed-in EL images of the marked-out areas in Fig. 7a are shown in Fig. 7b, c, and 7d. The marked-out areas in Fig. 7a are closer to the frame of the module and show the most critical hotspots. This is an indication of the occurrence of large leakage current during operation. There are other hotspots all over the module, however. The respective location of the hotspot cells closer to the frame of the PV module supports the observations in the EL images. The number of hotspot cells suggests that the majority of the cells in field-aged PV Module X are at different stages of degradation.

In Fig. 7b, no obvious crack was observed. Yet, the corresponding area in Fig. 7a shows hotspots. The observed hotspots in Fig. 7a might be due to metal grids corrosion and/or solar cell degradation. Fig. 7c shows the presence of microcracks and the warmest cells were observed in this area in the IR-T image, see Fig. 7a. On the other hand, Fig. 7d shows some cracks. However, the hotspots of its corresponding area in the IR-T image were not as high as the hotspots in Fig. 7c. The criticality of cracks to current flow underpins the occurrence and severity of the hotspots observed in Fig. 7c [25,26]. The ΔT of PV Module X was found to be ~8.2 ± 2 °C. The presence of MID products such as acetic acid, oxides and acetates of silver, lead, and copper could also influence the formation and the characteristics of the hotspots [12].

3.6. Microstructural characteristics

3.6.1. Solar cells

Fig. 8 shows the SEM micrographs of a multicrystalline silicon solar cell extracted from the edge of PV Module X. Fig. 8a shows two distinct surface morphology of the silicon microcrystal structures present in the solar cell. Area 1 appears to be the characteristic surface morphology of alkaline anisotropic etching of crystalline silicon [50]. On the other hand, Area 2 depicts the surface morphology of isotropic etching using acidic solutions [50]. As a multicrystalline silicon solar cell, the cell is made up of different crystals with random crystallographic orientations. It is known that etching rate depends on the etchant, crystal type and orientation. Hence, the crystal type and orientations might be the reason for the difference in the surface morphology in Fig. 8a.

According to Li et al. [51], in the presence of moisture and light, the EVA encapsulation can produce acidic or basic environments in the solar

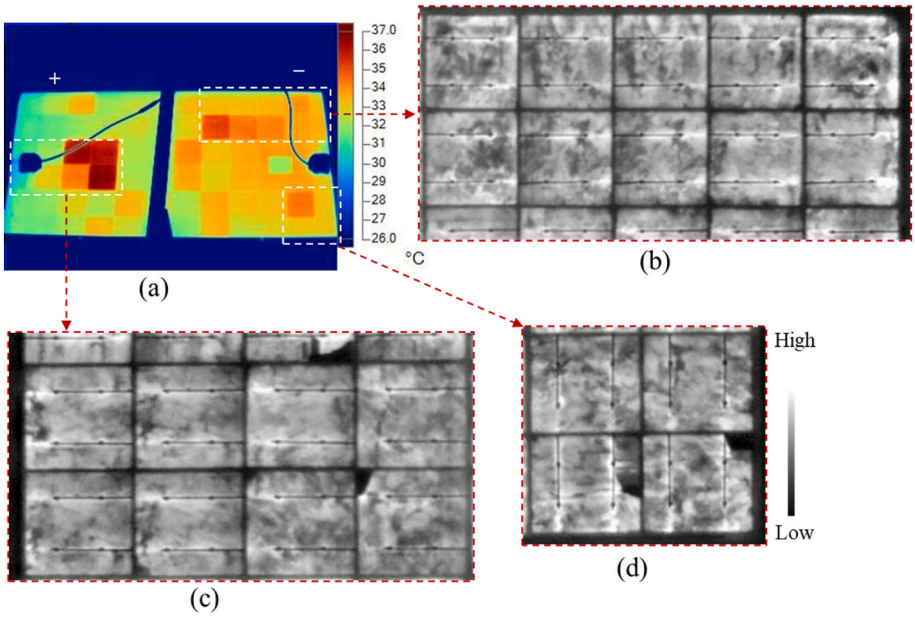

Fig. 7. (a) IR-T characteristics of PV Module X acquired under clear sky outdoor conditions. (b)–(d) EL characteristics acquired under I_{sc} bias conditions of the corresponding marked areas in (a).

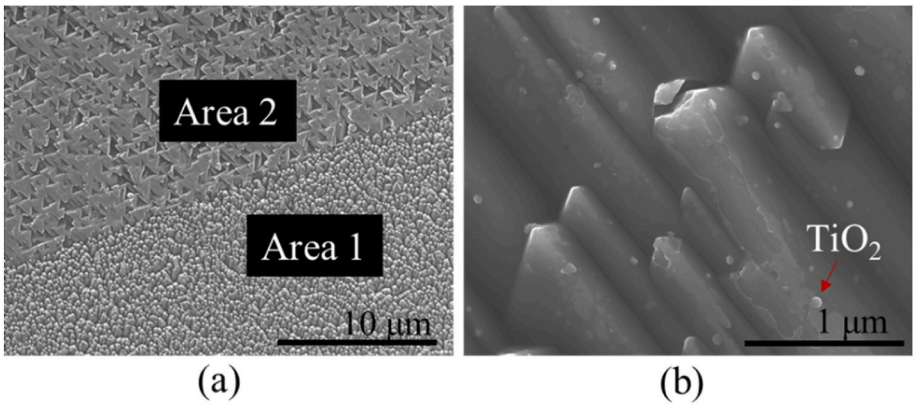

Fig. 8. SEM micrographs of a solar cell extracted from PV Module X showing (a) the types of micro crystallographic features and (b) high magnification micrograph of Area 1.

panel bulk depending on the voltage bias in the field. Under negative bias, as typical of solar panels affected by PID, the EVA under moisture ingress can produce basic environment in the panel. High basic environment can make degradation of the silicon solar cell, antireflection coating, and corrosion of the metal grids feasible. However, under negative bias, the effect of basic environments on the corrosion of Ag metallization is negligible [51]. Yet, the amount of moisture accumulation within the solar panel is the rate determining step for the resulting basic or acidic environment in the panel. Moreover, since the solar cells used for the present investigation were extracted from the edge of the module, the influence of voltage bias (i.e., PID) on the degradation mechanisms in the module cannot be ruled out. Fig. 6b shows that the module might be affected by PID. Therefore, it is likely that the EVA encapsulation degraded and provided both acidic and basic environments inside Module X. This suggests that degradation of different crystals in the solar cell to different degrees is possible. This is likely one of the reasons for the differences in the surface morphologies observed in Fig. 8a.

In the high-magnification micrograph of Area 1 (Fig. 8b), the state of the microcrystals of the solar cells is clearer. Some portions of the microcrystals have disintegrated and undergone morphological changes. In this situation, the consequences for parasitic resistance losses and power degradation cannot be ruled out. The role of moisture ingress in the degradation of the solar cell appears to be significant. The white particles in Fig. 8b are the titanium dioxide (TiO_2) ARCs used on the surface of the solar cells to optimize efficiency. The effect of moisture on the degradation of the TiO_2 ARCs in field-aged PV Module X was reported earlier [33]. The TiO_2 ARCs were found to be oxidized, highly porous, and aggregation of silver nanoparticles (NPs) on the surfaces of the TiO_2 ARC particles were observed. Hence, the formation of titania metal complexes (e.g., silver-titania and titania-alumina complexes) is feasible [33]. Degradation of the TiO_2 ARC due to moisture ingress in field deployed PV modules was also reported by Baldus-Jeursen et al. [23]. In addition, migration of metal ions to the surface of the ARC leads to leakage currents, and hence, PID [23,52].

Fig. 9 shows the SEM micrographs and EDS analyses of a solar cell extracted from the edge of the module. Fig. 9a and c are the respective SEM and EDS analyses acquired approximately 10 mm from the edge of the solar cell. In Fig. 9b and d, the SEM micrograph and EDS analysis taken from the edge of the cell are shown, respectively. The EDS

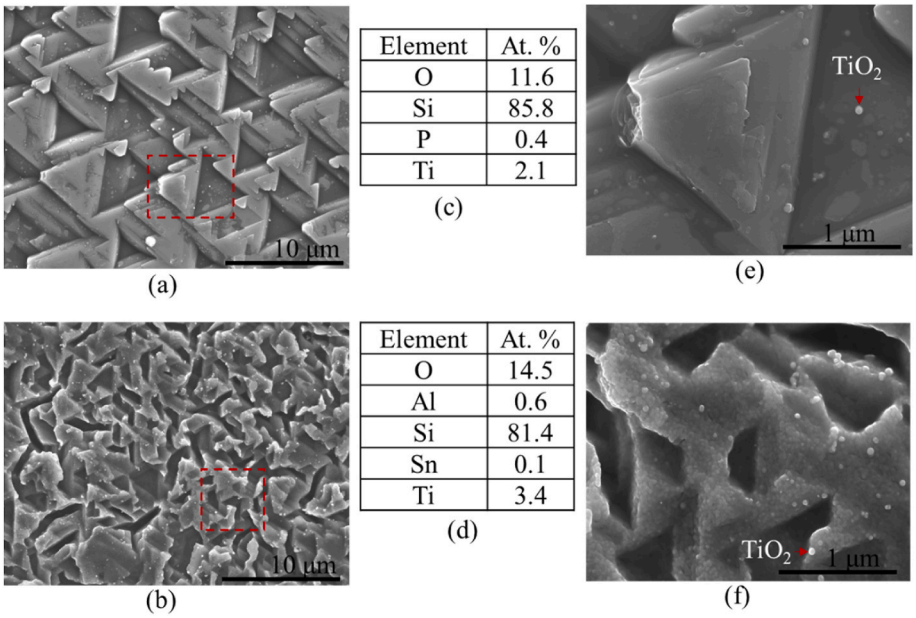

Fig. 9. SEM micrographs and EDS analyses of a solar cell extracted from the edge of PV Module X. (a)–(b) SEM micrographs and (c)–(d) EDS analyses acquired ca. 10 mm from the edge and just at the edge of the solar cell. SEM micrographs of the marked-out areas in (a) and (b) are shown in (e) and (f), respectively. The EDS analyses are represented in atomic % (at. %).

analyses show the composition of oxygen (O), silicon (Si), phosphorus (P), titanium (Ti), aluminum (Al), tin (Sn), and lead (Pb) in atomic % (at. %). Fig. 9e and f are the SEM micrographs of the marked-out areas in Fig. 9a and b, respectively. The microcrystal structures in Fig. 9a are similar to what was observed in Fig. 8a, Area 2. However, the microcrystal structures in Fig. 9b are completely different from what was observed in Fig. 8. The microcrystalline features of the solar cell in Fig. 9b appear to be more amorphous. The EDS analyses in Fig. 9c and d shows that the amount of oxygen is higher in the results acquired from the edge of the field-aged PV module. It is clear from Fig. 9e and f that the region of the solar cell in Fig. 9f is more amorphous than what is observed in Fig. 9e. The presence of oxygen in Fig. 9e and f suggests that there is a general trend of degradation across the solar cell. With these microcrystalline structures, poor charge carrier generation and high parasitic recombination in the solar cells is expected. This is likely one of the key factors for the observed degradation in P_{max} of the field-aged PV module, refer to Fig. 5. Phosphorus (P) in Fig. 9c is believed to come from the MID of the EVA encapsulation [23].

Phosphorus containing additives are used as secondary antioxidants to stabilize the encapsulation materials against peroxide degradation [13]. Hence, formation of phosphate compounds under the influence of moisture ingress is possible. At the edges and areas in the PV module where the influence of moisture ingress is more pronounced, formation of degradation compounds (e.g., Al_2O_3) is likely, see Fig. 9d. Formation of aluminum oxides due to the influence of moisture and acetic acid was also reported elsewhere [18]. More significantly, the number and proportion of chemical species increase in the EDS data acquired from the edge of the solar cell due to moisture ingress. For instance, the amount of Ti in Fig. 9c is less than what is observed in Fig. 9d. Migration and aggregation of TiO_2 nanoparticles (NPs) around the solar cell edges under the influence of moisture ingress is a possible explanation for this observation.

Fig. 9d shows the presence of Al and Sn. Aluminum can leach from the back contact of the cell or from the Al- frame of the PV module to the cell surface under the influence of moisture ingress [16,20]. Galvanic corrosion of the Al back contact, under the influence of moisture and acetic acid, causes optical degradation and deposits oxide films on the electrodes, especially around the solder joint [18]. This is because Al has the least potential (−1.662 V) among the metals in the Ag paste and solder material and is preferentially corroded in the presence of moisture and acetic acid [17,18].

According to Bai et al. [20], in the presence of moisture, Al ions are capable of migrating to the surface of the solar cell via hydrolysis. In addition, Sn from the solder or the tinned Cu ribbon can migrate under moisture ingress (Fig. 9d), as observed elsewhere [16]. This appears to confirm the observation that degradation is more severe around the edges and cracked areas of the PV module [12]. This is because moisture ingress takes place through microcracks, voids, and the edges of PV modules [4]. Fig. 10 shows the SEM-EDS elemental mappings of oxygen, sodium, silicon, titanium, and carbon, for a sample of the solar cell extracted from Module X. Fig. 10 suggests some amount of oxygen is present, which is one of the main moisture ingress species. That is, formation of chemical complexes between oxygen and the elements in Fig. 10 is feasible. Fig. 10c suggests that the migration of sodium (Na^+) ions under the influence of moisture ingress cannot be ruled out. The presence of these ions at the emitter regions of the solar cell leads to PID [9]. Also, the formation of sodium hydroxides and bicarbonates is possible. This observation agrees with the leaching behaviour of Na^+ ions in the presence of moisture reported by Smets and Lommen [53] and Hoffmann and Koehl [46]. Moisture induced migration of Na^+ ions lead to the solar cell degradation [24].

From Fig. 10b and d, distribution of oxygen across the surface of the cell can be observed. The black spots and traces around the pyramids of the Si microcrystals are the traces of oxidized TiO_2 ARC NPs around these areas. This was also observed elsewhere [16]. Fig. 10e also suggests that beside the TiO_2 ARC NPs, traces of Ti were observed across the cell area. The traces of carbon (Fig. 10f) indicate that the presence of acidic species e.g., acetic acid in the module is possible. EVA encapsulants produce acetic acid under the influence of moisture and light [4]. The presence of carboxylic acids led to further degradation of Si in these

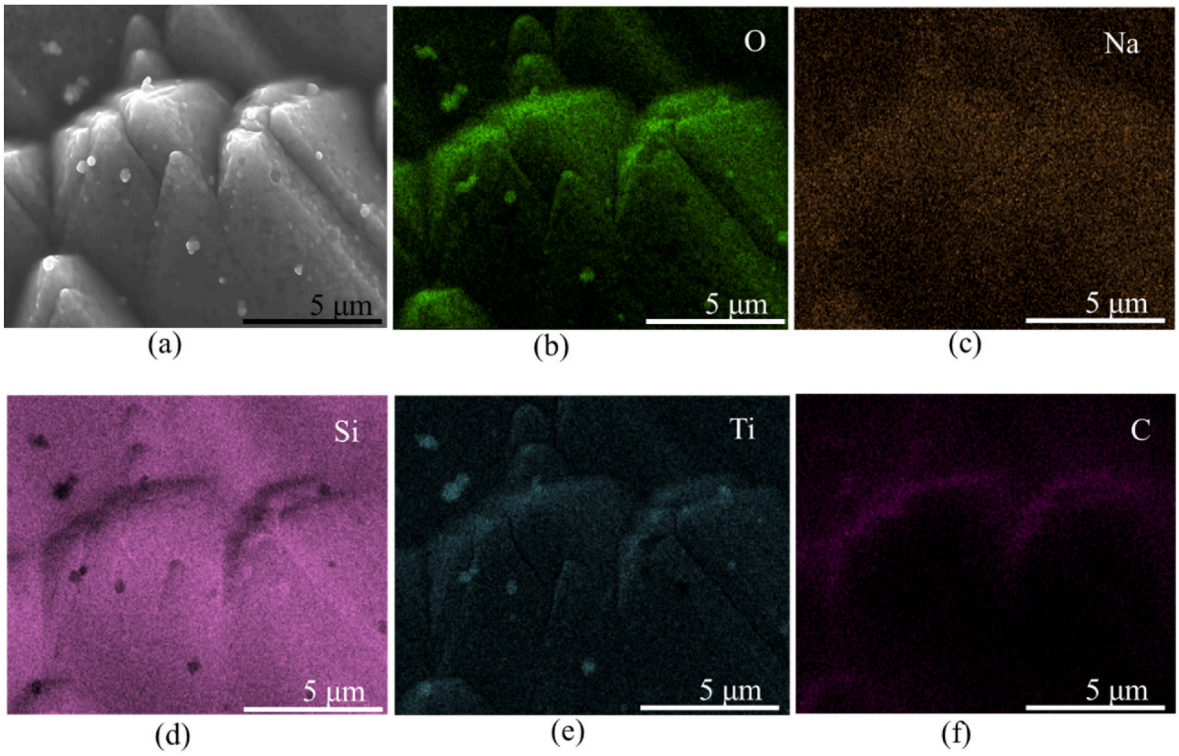

Fig. 10. (a) SEM micrograph and EDS element mappings of (b) oxygen, (c) sodium, (d) silicon, (e) titanium, and (f) carbon acquired from the edge of a solar cell extracted from PV Module X.

areas, see Fig. 10d and f.

The presence of carbon could also be due to the diffusion of carbon dioxide (CO_2) from the edge of the module or/and through cracks created in the module during field operation [4]. Fig. 11 shows the SEM micrograph and the respective EDS analyses of a cell area close to the Ag fingers of a solar cell extracted from the edge of Module X. The SEM micrograph in Fig. 11a suggests that the front surface of the solar cell and the Ag finger have undergone substantial degradation.

This observation is supported by the EDS full area analysis (Fig. 11b) and spot analyses in Fig. 12c and d. The presence and amount of oxygen in the EDS analysis in Fig. 11b suggest the influence of moisture ingress on the observed cell degradation. There is migration of cations of sodium, aluminum, lead, silver, potassium, and titanium to the surface of the solar cell under the influence of moisture ingress. Subsequently, the spot analysis of Point 1 shows that the silicon solar cell has been oxidized, see Fig. 11c. Interestingly, the amount of Si at Point 2 is the least due to the presence of C and O, see Fig. 11d. Moreover, the presence and amount of carbon in Point 2 indicates the presence of MID products of EVA such as acetic acid.

The release of chlorine and phosphorus in the degradation process of the EVA encapsulation material is also possible, see Fig. 11b. Not long ago, Kumar et al. [12] also observed about 0.28 atomic % of chlorine in a field-aged PV module that was deployed in India. The presence of moisture and acetic acid accounts for the observed degradation of the solar cell and Ag grid in Fig. 11a. Ingressed moisture activates the surface of the Ag followed by reaction of the activated Ag grid with acetic acid to form silver acetate [13,14,16]. The formation of silver acetate leads to optical degradation [27]. Fig. 12 shows the EDS mappings of oxygen, silicon, carbon, and phosphorus of the SEM micrograph in Fig. 11a.

Fig. 12a shows that oxygen is found across the surface of the solar cell. In Fig. 12b, it appears that Points 1 and 2 are at different vertical heights on the solar cell, compare with Fig. 11a. The Si mapping shows crevices or pits at the regions where carbon is present. The crevices appear dark in the EDS maps, see Fig. 12. These crevices appear to serve as reservoirs for moisture and MID products, refer to Fig. 11d. In that regard, acetic acid might accumulate and contribute to further degradation in the localized areas of Point 2 which can result in the observed crevices in Fig. 11. In addition, Fig. 12c shows that carbon is present across the surface of the solar cell, even on the Ag grids, except at Point 1 (as in Fig. 11a). Point 1 is therefore appears to have undergone full carboxylic acid degradation, and hence, the presence of carbon in these regions is negligible. This is because it is unlikely that the diffusion of moisture and its degradation species will be restricted to Point 2 (refer to Fig. 11a) alone. Furthermore, MID products such as Ag ions tend to absorb CO_2 to form their respective carbonates and acetates [13,54]. This could reduce the concentration of C at Point 1, and hence, could not be present in the EDS analyses of this area. Moreover, the production and accumulation of phosphorus across the solar cell-Ag grid boundary is consistent, see Fig. 12d. It is believed that MID processes of the solar cell and the encapsulation release phosphorus to form silver phosphates [13]. In addition, the accumulation of phosphorus at the cell-Ag grid boundary is greatest nearer to Point 1 (where C is absent). Production and accumulation of phosphorous in the PV module can be correlated to the degree of EVA encapsulation degradation in the presence of moisture [8,55]. The silver phosphates (Ag_3PO_4) degradation products lead to optical degradation [13,55].

3.6.2. *Degradation of the silver grids*

One of the most important components of the solar cell is the silver grids: fingers and busbars, refer to Fig. 2. Yet, the Ag grids are prone to degradation in the presence of moisture and acetic acid [13,14,17]. Fig. 13 shows the SEM micrographs and EDS spectra of the Ag finger grid on a newly acquired commercial mc-Si solar cell. Trace amounts of

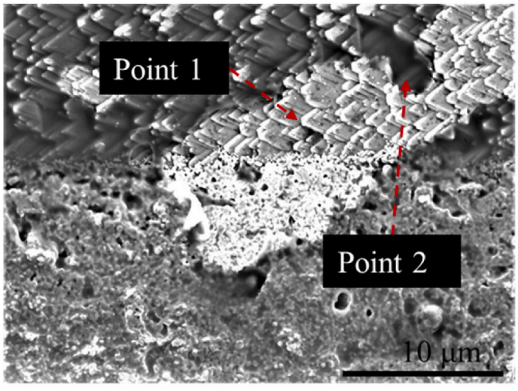

(a)

(b)

Element	At. %
O	20.8
Na	3.6
Al	0.5
Si	54.4
P	1.0
Pb	0.4
Cl	0.3
Ag	16.7
K	0.4
Ti	1.7

Point 1

Element	At. %
O	15.0
Al	0.6
Si	82.6
Sn	0.1
Ti	1.8

(c)

Point 2

Element	At. %
C	38.2
O	9.9
Na	0.2
Al	0.6
Si	49.6
Ti	1.5

(d)

Fig. 11. (a) SEM micrograph of front surface of solar cell and (b) EDS analyses of the full area of SEM micrograph in (a). (c) Point 1, and (d) Point 2 of the Ag–Si region of a solar cell extracted from the edge of the field-aged PV module showing degradation of the solar cell and the Ag finger.

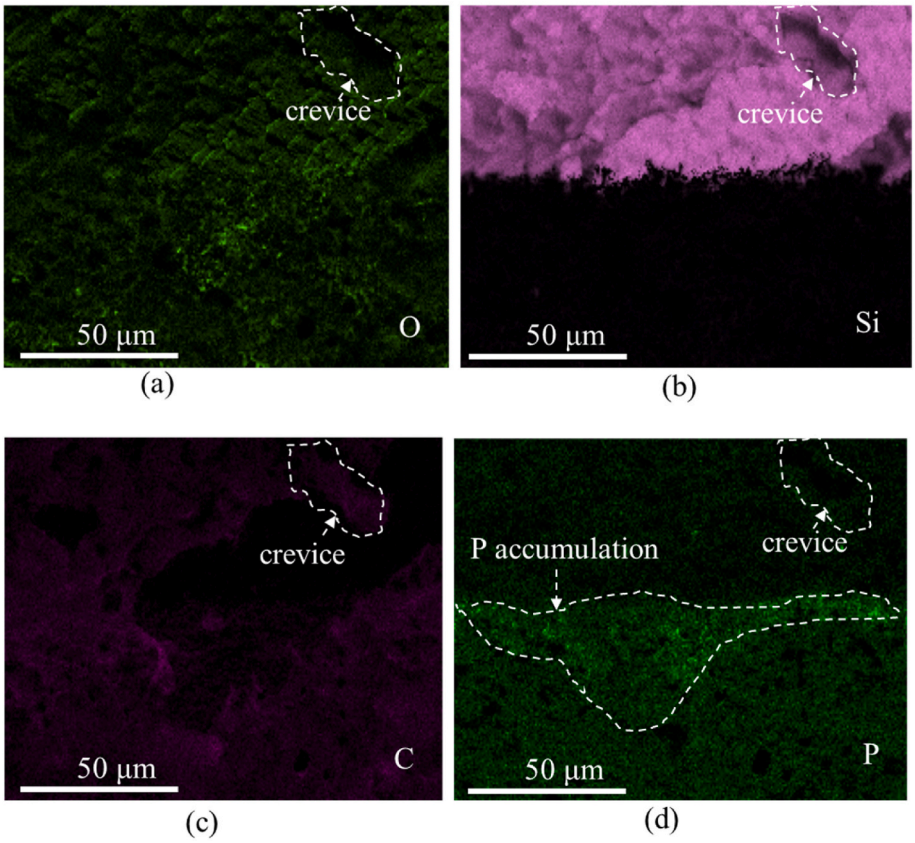

Fig. 12. EDS element mappings of (a) oxygen, (b) silicon, (c) carbon, and (d) phosphorus of the SEM micrograph in Fig. 11a.

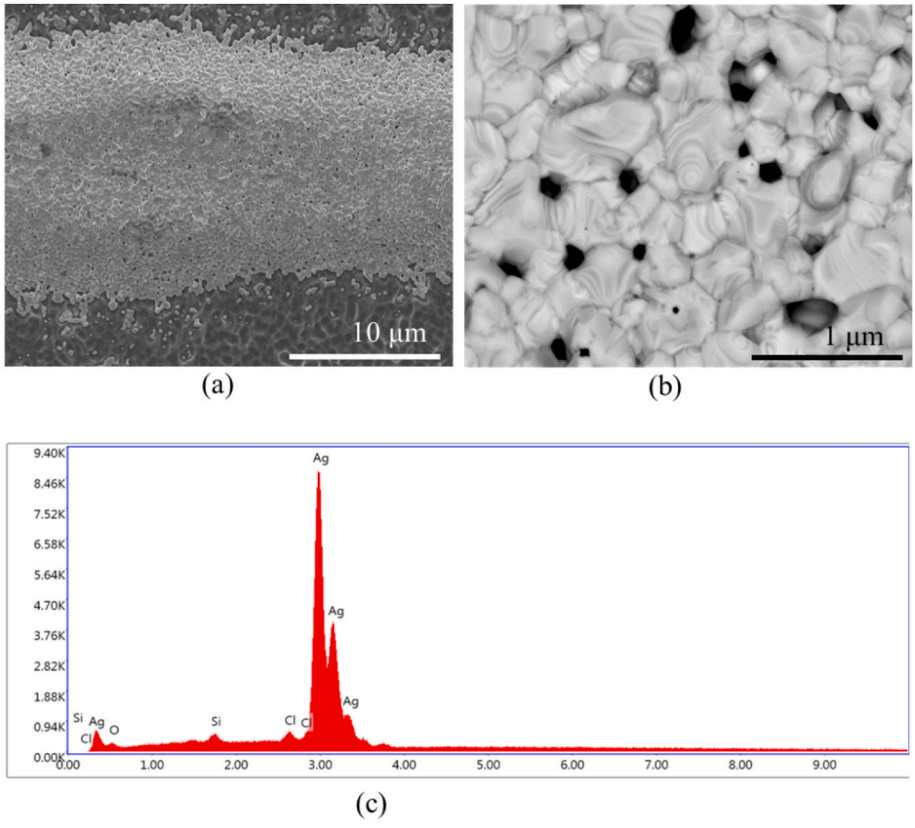

Fig. 13. (a)–(b) SEM micrographs of the Ag finger grid on a newly acquired commercial multicrystalline silicon solar cell and (c) EDS spectra of (b).

impurity Cl and O in Fig. 13c comes from the silicon production process.

In Fig. 13b, the morphology of the Ag grid shows a compact and well-ordered microstructure. The neck of the Ag micro-clusters is thicker as compared to the pore sizes. The pore density of the Ag micro-clusters is low as well. Fig. 14 shows the SEM micrographs and the EDS analysis of the Ag finger of a solar cell extracted from the edge of field-aged PV Module X. Fig. 14a and b shows the morphologies of the Ag grid of the solar cell and the EDS analysis is shown in Fig. 14c. The microstructure of the Ag grid in Fig. 14a is coarser than what is observed in Fig. 13a. Also, the neck of the Ag micro-clusters in this case are thinner and irregular, see Fig. 14b. The pore density is also higher as compared to what was observed in Fig. 13b. In addition, white micro crystallites were observed on the Ag NPs. These white crystallites are expected to be the acetates of silver or lead. These observed morphological changes agree with other reports in literature [13,14]. Duerr et al. [13] observed coarse Ag finger grids, white silver acetate crystals, and more porous Ag clusters in crystalline silicon modules affected by snail trails.

Jeffries et al. [14], observed thinner Ag cluster necks, larger and more pores, and irregular bumps, and white spot crystallites after a commercial Ag paste was subjected to 3000 h of acetic acid exposure. Moreover, Fig. 14c suggests that the Ag grids have been oxidized. This suggests that the formation of zinc, silicon, lead, and silver oxides is feasible. Fig. 15 shows the SEM micrographs and EDS analyses of the Ag busbar (refer to Fig. 2) of a solar cell extracted from the field-aged PV module. The analysis was carried out in the region nearer to the solder joint of the solar cell.

Fig. 15a shows that degradation of the Ag grid is possibly minimal. However, the EDS analysis of Fig. 15a suggests that Ag_2O is the main degradation product, see Fig. 15c. Fig. 15b is the SEM micrograph of the marked-out area in Fig. 15a, which highlights the degradation of the Ag grid better. This observation is supported by the corresponding EDS analysis in Fig. 15d, where the main degradation product expected in this area is AgO. A further EDS analysis at Point 1 in Fig. 15b suggests that the Ag grid could be present in a more severe degraded form, see Fig. 15e. The presence of fluorine in the EDS analysis in Fig. 15e might be coming from the degradation of the EVA encapsulant. The migration of Na, Al, and Pb to the surface of Ag grid is due to moisture ingress, as observed elsewhere [12,13,15–17,19]. Zinc, a component of Ag paste, is one of the degradation products responsible for optical degradation [13,28]. Zinc oxide (ZnO) was reported to be the intermediate compound for the formation of silver carbonate and silver hydroxide [54]. In this reaction mechanism, ZnO catalyzes the adsorption of ingressed CO_2 onto the Ag grid [13,54,56]. CO_2 could also be the byproduct of EVA degradation [4,13].

It was reported that under the influence of moisture, Ag has affinity for phosphorus, silicon, and sulfur [55]. Fig. 16 shows the SEM-EDS element mappings of oxygen, sodium, sulfur, lead, and zinc of the Ag busbar around the solder joint. The SEM micrograph in Fig. 16a shows a degradation trend similar to what was observed in Fig. 15b. The observed degradation is likely due to the presence of moisture and MID species on the Ag busbar region. The EDS element maps suggest that the formation of the oxides and sulfides of sodium, lead, and zinc cannot be ruled out.

Secondary organosulfur antioxidants, adhesion promoters, and stabilizers are used in the processing and/or stabilization of PV module backsheets [8,13,55]. These encapsulation materials release sulfur and phosphorus under the influence of moisture, and hence, lead to the formation of metal sulfides and phosphates [55]. These chemical species are highly photosensitive and can influence the opto-electrical characteristics of the PV module. The presence of oxygen and cell cracks can accelerate the formation of Ag_2S, and subsequent optical degradation [13,55]. In the visual inspection, it was observed that the field-aged PV module has undergone optical degradation. This observation is in line with the report by Duerr et al. [13]. Photosensitive Ag_2S appears as dark and hotspots in EL/UV-F and IR-T images, respectively.

3.6.3. Degradation of the copper ribbons

Fig. 17 shows the SEM micrographs and EDS analyses of the top and rear surfaces of the tinned Cu ribbon extracted from the field-aged PV module. The surface of the Cu ribbon is seen with microcracks which accelerate moisture ingress and degradation, see Fig. 17a. The observed oxidized layers along the crack contours suggest the influence of moisture ingress. It also indicates the role of moisture ingress in the development of microcracks. Cracks on Cu ribbons during thermal cycling has been observed and reported previously [15,57,58]. Point 1 shows erosion of the tin-plated surface on the Cu ribbon, see Fig. 17a. The EDS analysis of this region is shown in Fig. 17b indicating the presence of Cu. The EDS analysis of Point 2 shows the 'uneroded' surface of the tin-plated Cu ribbon in Fig. 17c, in which Cu is absent. The amount of Sn in Fig. 17b is higher than the amount of Sn in Fig. 17c. On the other hand, the amount of oxygen, silicon and lead are higher in Fig. 17c. In the first place, migration of O, Na, Ti, Si, and Pb elements to the surface of tinned Cu ribbon is normally due to moisture ingress. The amount of oxygen in Fig. 17b and c suggests that the surfaces of the tinned Cu ribbon are more oxidized due to the formation of surface oxide layers of Sn and Pb in the presence of moisture. That is, Sn and Pb of the tinned plated component of the Cu ribbon were oxidized preferentially to protect the Cu ribbon from degradation. This is likely the reason for the lower amount of Sn observed in Fig. 17c. However, when a large chunk of the protective oxidized Sn is removed, Cu could be found in a greater amount with lesser amount of oxygen, see Fig. 17b. Fig. 17d is the SEM micrograph of the rear surface of the tinned Cu ribbon and the corresponding EDS analysis is shown in Fig. 17e. The SEM-EDS analyses of the rear surface of the Cu ribbon suggest that this region has also undergone degradation due to moisture ingress.

The substantial amount of oxygen, aluminum, and the presence of carbon suggest the effect of moisture ingress and subsequent formation of carboxylic acids in this region. The presence of moisture together with acetic acid means that the formation of copper oxides, hydroxides, and acetates is feasible. In addition, the formation of metal complexes such

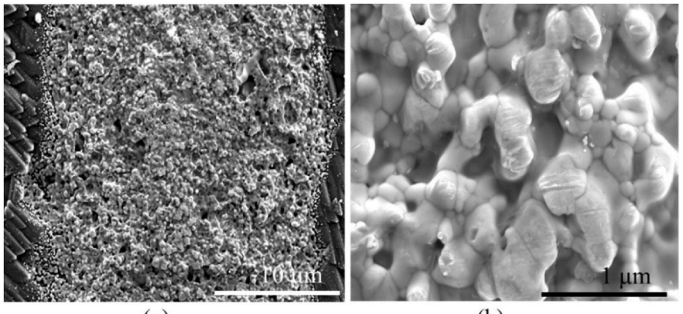

(a) (b)

Element	At. %
O	39.5
Zn	3.1
Si	2.7
Pb	0.7
Ag	54.0

(c)

Fig. 14. (a)–(b) SEM micrographs of the Ag finger of a solar cell extracted from the edge of the field-aged PV module and (c) EDS analysis of the SEM micrograph in (b).

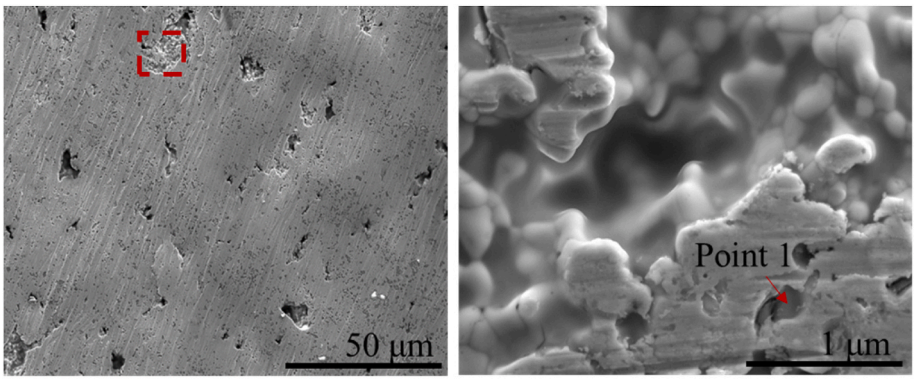

(a) (b)

Element	At. %
O	34.0
Na	8.5
Al	1.1
Si	2.3
Pb	0.8
Ag	53.4

(c)

Element	At. %
O	43.1
Si	2.6
Pb	1.4
Ag	48.5
Zn	4.4

(d)

Point 1

Element	At. %
O	60.9
F	1.7
Al	0.4
Si	6.5
Pb	4.0
Ag	14.3
Zn	12.3

(e)

Fig. 15. (a) SEM micrograph of the Ag busbar from the region nearer to the solder joint of the field-aged solar cell. (b) High magnification SEM micrograph of the marked-out area in (a). (c)–(e) EDS analyses of the SEM micrograph areas in (a), (b), and point analysis at Point 1, respectively.

as copper stannates and silver stannates around this region cannot be ruled out. These complexes have detrimental effect on the optoelectrical properties of the PV module [57].

Other competing reactions in this region can lead to the formation of aluminum and lead oxides and hydroxides [18]. In addition, it was observed that more elements were found on the rear surface of the Cu ribbon, see Fig. 17e. It is expected that these species migrated to the rear surface of the Cu ribbon under the influence of moisture ingress. However, the ratios of oxygen and copper in Fig. 17b and e are approximately 2:1 in both cases. This suggests that the degradation of the Cu ribbon in the PV module under the influence of moisture ingress is similar.

Fig. 18 shows the SEM-EDS analyses of the Ag busbar (refer to Fig. 2) of a solar cell at the solder joint extracted from the field-aged PV module. During PV module fabrication, the solar cells are stringed together with the Ag busbar underneath the Cu ribbon. SEM-EDS analyses were acquired from the region of the Ag busbar at the solder joint of the solar cell. Fig. 18a shows that after the Cu ribbon was detached from the solar cell, a large chunk of the tinned Cu ribbon remained on the solar cell and masked out the Ag busbar. This suggests that the Cu ribbon has undergone degradation leaving behind significant remnants of the tinned Cu ribbon. In this case, the possible influence of moisture ingress in the Cu ribbon degradation cannot be ruled out. This is supported by the presence and amount of copper, tin, and oxygen in the EDS analysis, see Fig. 18b.

Degradation of the Cu ribbon might also be accelerated by the presence of acetic acid, as observed in Fig. 17d and e. The Cu ribbon degradation due to the presence of acetic acid was reported elsewhere [15–17,27]. Formation of oxides of copper, tin, lead, aluminum, and silver in such areas is feasible, and underlines parasitic resistance losses.

3.6.4. Degradation of the solder bonds

Fig. 19 shows the SEM-EDS analyses of the solder bond in the solar cell extracted from the field-aged PV module. Fig. 19a shows the SEM micrograph and Fig. 19b shows the corresponding EDS analysis of the SEM micrograph in Fig. 19a. Fig. 19 indicates that the major component of the solder is lead and tin. Apart from Pb and Sn, migration of chemical species under the influence of moisture ingress is the reason for the observed oxygen, sodium, aluminum, silver, calcium, and copper in Fig. 19b. Point analyses for Pb and Sn in Fig. 19a show that Pb was more oxidized. The amount of oxygen at areas where Pb was observed was higher than areas where Sn was observed (not shown here). Yet, Sn remained largely unoxidized, even though Sn has lower potential.

It is known that solder degradation in the presence of moisture and acetic acid obeys the galvanic corrosion reaction [17,18]. In the presence of moisture and acetic acid, Pb is preferentially corroded [59]. Acetic acid catalyzes the degradation of the Pb in the solder in the presence of moisture [60]. Under atmospheric conditions, a nanometer sized protective lead oxide passive layer is formed on the surface of Pb according to the following reaction mechanisms:

$$\text{Anode (oxidation)} : Pb \rightarrow Pb^{+2} + 2e^{-} \quad (1)$$

$$\text{Cathode (reduction)} : \frac{1}{2}O_2 + H_2O + 2e^{-} \rightarrow 2OH^{-} \quad (2)$$

$$\text{Passive PbO layer} : Pb^{+2} + 2OH^{-} \rightarrow PbO + H_2O \quad (3)$$

The passivation lead oxide (PbO) layer protects the Pb metal from further corrosion and degradation. However, in the presence of moisture and acetic acid, the PbO protective layer is susceptible to dissolution, and hence, degradation. The acidified electrolyte (consisting of several MID products) in the PV module permeates into cracks and defects in the PbO protective layer and reacts with the Pb to form soluble lead acetate complexes according to the following reaction mechanisms [61]:

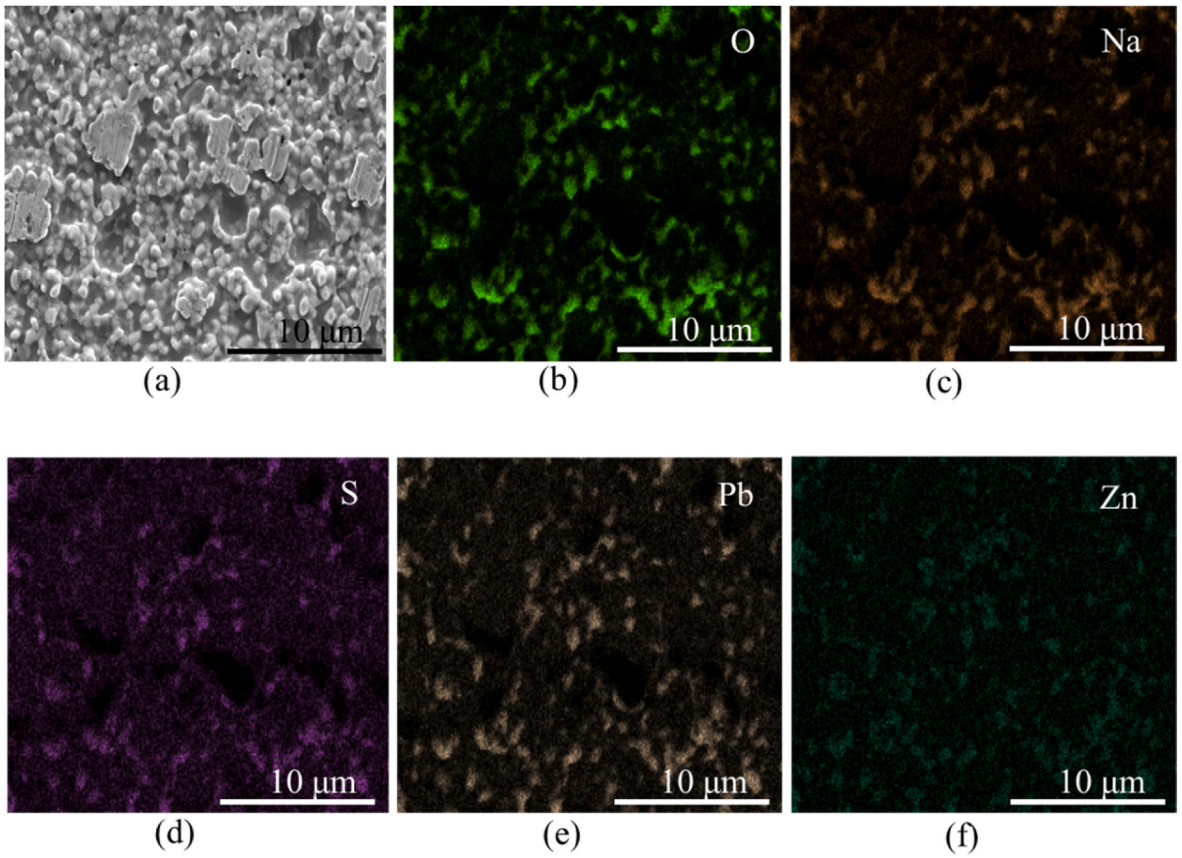

Fig. 16. (a) SEM micrograph and EDS element mappings of oxygen (O), sodium (Na), sulfur (S), lead (Pb), and zinc (Zn) of the Ag busbar at the solder joint of the extracted solar cell.

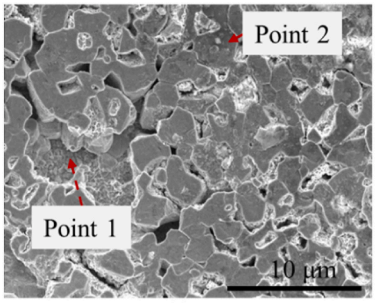

Point 1

Element	At. %
Ti	6.2
O	37.9
Si	6.6
Pb	5.7
Sn	25.5
Cu	18.1

(b)

Point 2

Element	At. %
O	66.7
Na	5.2
Si	9.3
Pb	16.6
Sn	2.3

(c)

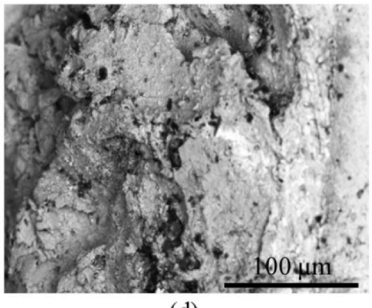

Element	At. %
C	6.9
O	45.7
Cu	25.1
Al	4.1
Si	2.3
Pb	8.9
Sn	7.0

(e)

Fig. 17. (a) SEM micrograph of the top surface of the Cu ribbon and the corresponding EDS analyses of (b) Point 1 and (c) Point 2. (d) SEM micrograph and (e) corresponding EDS analysis of the rear surface of the Cu ribbon. Data was acquired from the field-aged PV module.

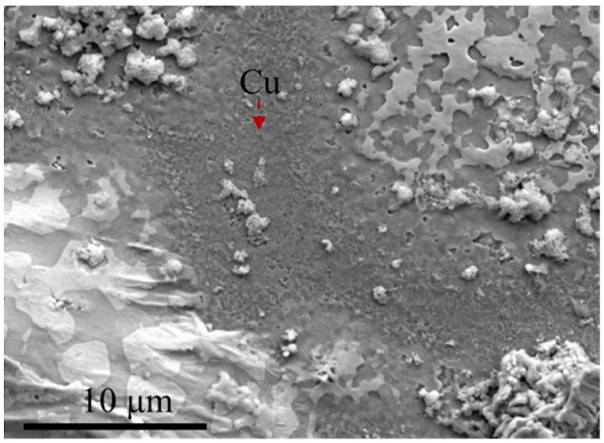

Element	At. %
O	19.3
Al	3.1
Pb	7.8
Ag	2.2
Sn	22.0
Cu	45.4

(b)

Fig. 18. (a) SEM micrograph and (b) EDS analysis of the Ag busbar beneath the Cu ribbon of the solar cell at the solder joint extracted from the PV module.

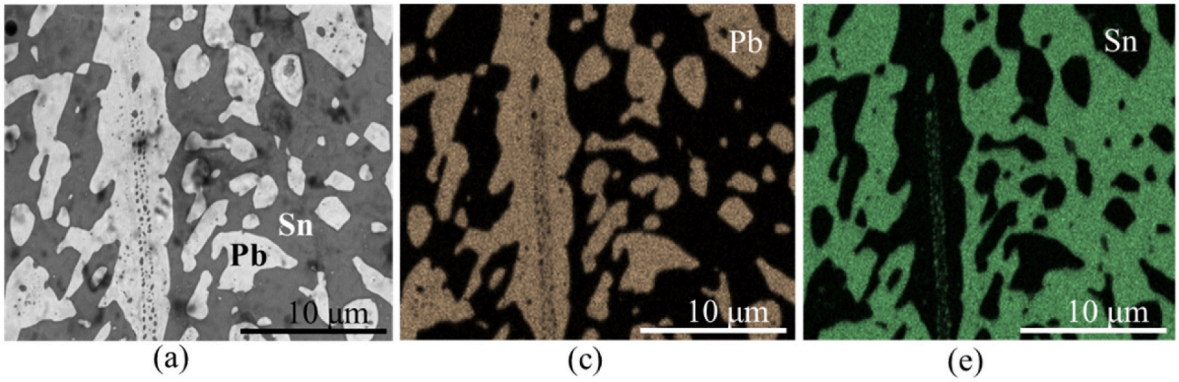

(b)

Element	At. %
O	10.7
Na	1.8
Al	0.3
Si	2.3
Pb	20.6
Ag	1.1
Sn	60.6
Ca	2.5
Cu	0.2

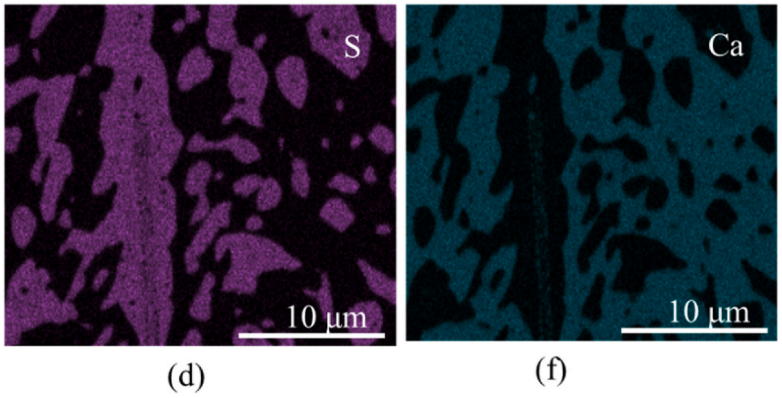

Fig. 19. (a) SEM micrograph and (b) EDS analyses of the solder bond in the solar cell extracted from the field-aged PV module. EDS element mappings of (c) lead, (d) sulfur, (e) tin, and (f) calcium indicating formation of metal complexes due to moisture ingress.

$$\text{PbO layer dissolution}: PbO + 2CH_3COOH \rightarrow Pb^{+2} + 2CH_3COO^{-} + H_2O \quad (4)$$

$$2PbO + Pb^{+2} + 2CH_3COO^{-} + H_2O \rightarrow Pb(CH_3COO)_2 \bullet 2PbO \bullet H_2O \quad (5)$$

To understand other competing reactions, elemental maps were acquired from Fig. 19a. It was observed that the mappings of Pb and sulfur were similar, see Fig. 19c and d. On the other hand, the mappings of Sn and calcium were also similar, see Fig. 19e and f. Interestingly, the elemental mappings of the minor elements (e.g., Na, Al, Si, P, and Cu) were similar to the mappings of Pb and sulfur. These elemental mappings suggest that the formation of lead sulfides and phosphates is feasible. Formation of other Sn-metal complexes such as calcium, copper, and sodium stannates is also expected, see Fig. 19e and f.

Taken together, moisture ingress is the underlying factor for the formation of oxides, hydroxides, sulfides, phosphates, acetates, and carbonates of silver, lead, tin, copper, zinc, and aluminum in the field-aged PV modules. Notably, moisture can induce the formation of photosensitive metal-ligand complexes of silver, tin, and titanium. The solar cells also undergo consequential degradation when exposed to moisture and its degradation products. These MID products lead to the observed corrosion, cracks, optical degradation, and PID in the field-

aged PV module. Subsequently, these defects and fault modes cause parasitic resistance losses, and hence, power degradation in the field-aged PV module.

4. Conclusion

In the present work, the effect of moisture ingress on the degradation of reclaimed solar cells from a 20-year-old field-aged mc-Si PV module was investigated. Visual inspection, I–V characterization, EL, UV-F, and IR-T imaging techniques show that the PV module has undergone substantial degradation. To elucidate the role of moisture ingress on the observed degradation mechanisms, microstructural analyses were conducted on the extracted solar cells from the PV module using SEM-EDS techniques. Visual inspection demonstrated that the EVA encapsulation has undergone optical degradation and the extracted cells show dark discolored TPT backsheets. Corrosion at the solder joint was dominant and is attributed to the dissolution of lead and tin (main components of solder) and the Ag grids in moisture and acetic acid due to galvanic corrosion.

Moisture ingress, in the presence of light, in the field-aged PV module led to the degradation of the EVA encapsulation, and hence, the formation of carboxylic acids such as acetic acid and degradation products such as CO, CO_2, phosphorus, sulfur, fluorine, and chlorine. In the presence of moisture and acetic acid, the solar cells, metal grids, solder bonds, and the antireflection coatings undergo different forms of degradation. The solar cell and ARC become oxidized under the influence of moisture ingress. Moisture ingress influences the migration of metal ions e.g., Na, Ag, Pb, Sn, Cu, Zn, and Al to the surface of the solar cells, and hence, leads to PID. Silver and zinc ions originate from the degradation of the silver paste used for the Ag grids and busbars. Whilst Pb and Sn ions come from the solder, the copper ribbon is the source of Cu and also Sn ions. The Al and Na ions migrate from the Al- frame and/or rear solar cell contact and the soda lime front glass, respectively.

In this regard, the formation of oxides, hydroxides, sulfides, phosphates, acetates, and carbonates of silver, lead, tin, copper, zinc, and aluminum have been observed. Degradation of the front and rear surfaces of the copper ribbons appears to be similar. However, degraded remnants of the Cu ribbon can mask out the silver busbar, leading to parasitic resistive losses. Also, other competing reactions can lead to the formation of stannates of copper, silver, sodium, and zinc. Similarly, migration of silver and aluminum to the surfaces of the TiO_2 ARC NPs can lead to the formation of titania-alumina and silver-titania complexes. It was observed that, in the presence of moisture and acetic acid, Pb is preferentially corroded (to form lead acetate complexes) instead of the expected sacrificial Sn in the solder.

These MID species may account for the observed metal grids corrosion, cell cracks, optical degradation, and PID in the field-aged PV module. In the EL and UV-F images, these degradation species appear as dark spots, and as hotspots in IR-T images. It is well known that these defects and fault modes can lead to parasitic resistance losses which was witnessed by the overall 1.2%/year degradation in the P_{max} of the field-aged PV module. The relative temperature coefficient of efficiency of the examined PV module was found to be −0.5%/°C. In a Nordic environment with high CMI, the role of these MID mechanisms in the degradation of field-aged solar PV modules is very significant. Investigation of MID mechanisms in field-aged solar PV modules is more reflective of the reality in the field. Though solar PV module materials and technology have evolved over the years, MID mechanisms in solar PV modules appear to follow a similar trend. Hence, insights from this work can guide decision making at the present and in the future as regards understanding the performance reliability of solar PV plants.

CRediT authorship contribution statement

Oscar Kwame Segbefia: Writing – original draft, Validation, Methodology, Investigation, Formal analysis, Conceptualization. **Naureen Akhtar:** Writing – review & editing, Validation, Investigation, Formal analysis. **Tor Oskar Sætre:** Writing – review & editing, Supervision, Funding acquisition, Conceptualization.

Declaration of competing interest

The authors declare that they have no known competing financial interests or personal relationships that could have appeared to influence the work reported in this paper.

Data availability

Data will be made available on request.

Acknowledgement

The authors acknowledge the continuous support of the University of Agder, Norway and Dr. Odin Kvam of the Department of Engineering Sciences, University of Agder for his role in the solar cell samples' reclamation for this investigation.

References

[1] A. Dadaniya, N.V. Datla, Water diffusion simulation in photovoltaic module based on the characterization of encapsulant material using in-situ gravimetric technique, Sol. Energy Mater. Sol. Cell. 201 (2019), 110063.
[2] C. Han, Analysis of moisture-induced degradation of thin-film photovoltaic module, Sol. Energy Mater. Sol. Cell. 210 (2020), 110488.
[3] M.D. Kempe, Modeling of rates of moisture ingress into photovoltaic modules, Sol. Energy Mater. Sol. Cell. 90 (2006) 2720–2738.
[4] O.K. Segbefia, A.G. Imenes, T.O. Sætre, Moisture ingress in photovoltaic modules: a review, Sol. Energy 224 (2021) 889–906.
[5] O.K. Segbefia, N. Akhtar, T.O. Sætre, Defects and fault modes of field-aged photovoltaic modules in the Nordics, Energy Rep. 9 (2023) 3104–3119.
[6] N. Kim, C. Han, Experimental characterization and simulation of water vapor diffusion through various encapsulants used in PV modules, Sol. Energy Mater. Sol. Cells 116 (2013) 68–75.
[7] D. Wisniewski, R. Lv, S.V. Nair, J.N. Jaubert, T. Xu, H.E. Ruda, Measurement and modelling of water ingress into double-glass photovoltaic modules, Prog. Photovoltaics Res. Appl. 27 (2019) 144–151.
[8] C. Peike, S. Hoffmann, P. Hulsmann, B. Thaidigsmann, K.A. Weiss, M. Koehl, P. Bentz, Origin of damp-heat induced cell degradation, Sol. Energy Mater. Sol. Cells 116 (2013) 49–54.
[9] V. Naumann, D. Lausch, A. Hahnel, J. Bauer, O. Breitenstein, A. Graff, M. Werner, S. Swatek, S. Grosser, J. Bagdahn, C. Hagendorf, Explanation of potential-induced degradation of the shunting type by Na decoration of stacking faults in Si solar cells, Sol. Energy Mater. Sol. Cell. 120 (2014) 383–389.
[10] C.J. Willmott, J.J. Feddema, A more rational climatic moisture index, Prof. Geogr. 44 (1992) 84–88.
[11] S. Mitterhofer, C. Barretta, L.F. Castillon, G. Oreski, M. Topic, M. Jankovec, A dual-transport model of moisture diffusion in PV encapsulants for finite-element simulations, IEEE J. Photovoltaics 10 (2020) 94–102.
[12] S. Kumar, R. Meena, R. Gupta, Imaging and micro-structural characterization of moisture induced degradation in crystalline silicon photovoltaic modules, Sol. Energy 194 (2019) 903–912.
[13] I. Duerr, J. Bierbaum, J. Metzger, J. Richter, D. Philipp, Silver grid finger corrosion on snail track affected PV modules–investigation on degradation products and mechanisms, Energy Proc. 98 (2016) 74–85.
[14] A.M. Jeffries, T. Nietzold, L.T. Schelhas, M.I. Bertoni, Corrosion of novel reactive silver ink and commercial silver-based metallizations in diluted acetic acid, Sol. Energy Mater. Sol. Cells 223 (2021), 110900.
[15] J.S. Jeong, N. Park, C. Han, Field failure mechanism study of solder interconnection for crystalline silicon photovoltaic module, Microelectron. Reliab. 52 (2012) 2326–2330.
[16] N. Kyranaki, A. Smith, K. Yendall, D.A. Hutt, D.C. Whalley, R. Gottschalg, T. R. Betts, Damp-heat induced degradation in photovoltaic modules manufactured with passivated emitter and rear contact solar cells, Prog. Photovoltaics Res. Appl. 30 (9) (2022) 1061–1071.
[17] T.H. Kim, N.C. Park, D.H. Kim, The effect of moisture on the degradation mechanism of multi-crystalline silicon photovoltaic module, Microelectron. Reliab. 53 (2013) 1823–1827.
[18] H.P. Xiong, C.H. Gan, X.B. Yang, Z.G. Hu, H.Y. Niu, J.F. Li, J.F. Si, P.F. Xing, X. T. Luo, Corrosion behavior of crystalline silicon solar cells, Microelectron. Reliab. 70 (2017) 49–58.
[19] W. Oh, S. Kim, S. Bae, N. Park, Y. Kang, H.-S. Lee, D. Kim, The degradation of multi-crystalline silicon solar cells after damp heat tests, Microelectron. Reliab. 54 (2014) 2176–2179.

[20] Q. Bai, H. Yang, C. Nan, H. Wang, Z. Chen, Analysis of the electrochemical reactions and ions migration for crystalline silicon solar module under high system voltage, Sol. Energy 225 (2021) 718–725.
[21] O.K. Segbefia, T.O. Sætre, Investigation of the temperature sensitivity of 20-years old field-aged photovoltaic panels affected by potential induced degradation, Energies 15 (2022) 3865.
[22] E.L. Meyer, E.E. Van Dyk, Assessing the reliability and degradation of photovoltaic module performance parameters, IEEE Trans. Reliab. 53 (2004) 83–92.
[23] C. Baldus-Jeursen, A. Côté, T. Deer, Y. Poissant, Analysis of photovoltaic module performance and life cycle degradation for a 23 year-old array in Quebec, Canada, Renew. Energy 174 (2021) 547–556.
[24] K. Matsuda, T. Watanabe, K. Sakaguchi, M. Yoshikawa, T. Doi, A. Masuda, Microscopic degradation mechanisms in silicon photovoltaic module under long-term environmental exposure, Jpn. J. Appl. Phys. 51 (2012) 10NF07.
[25] M. Köntges, S. Kurtz, C. Packard, U. Jahn, K.A. Berger, K. Kato, T. Friesen, H. Liu, M. Van Iseghem, J. Wohlgemuth, Review of Failures of Photovoltaic Modules, 2014.
[26] U. Jahn, M. Herz, M. Köntges, D. Parlevliet, M. Paggi, I. Tsanakas, Review on Infrared and Electroluminescence Imaging for PV Field Applications: International Energy Agency Photovoltaic Power Systems Programme: IEA PVPS Task 13, International Energy Agency, 2018. Subtask 3.3: report IEA-PVPS T13-12: 2018.
[27] N. Iqbal, D.J. Colvin, E.J. Schneller, T.S. Sakthivel, R. Ristau, B.D. Huey, X. Ben, J.-N. Jaubert, A.J. Curran, M. Wang, Characterization of front contact degradation in monocrystalline and multicrystalline silicon photovoltaic modules following damp heat exposure, Sol. Energy Mater. Sol. Cells 235 (2022), 111468.
[28] P. Peng, A. Hu, W. Zheng, P. Su, D. He, K.D. Oakes, A. Fu, R. Han, S.L. Lee, J. Tang, Microscopy study of snail trail phenomenon on photovoltaic modules, RSC Adv. 2 (2012) 11359–11365.
[29] O. Dupré, R. Vaillon, M.A. Green, Physics of the temperature coefficients of solar cells, Sol. Energy Mater. Sol. Cells 140 (2015) 92–100.
[30] S. Kumar, R. Meena, R. Gupta, Finger and interconnect degradations in crystalline silicon photovoltaic modules: a review, Sol. Energy Mater. Sol. Cells 230 (2021), 111296.
[31] M.C.C. de Oliveira, A.S.A.D. Cardoso, M.M. Viana, V.d.F.C. Lins, The causes and effects of degradation of encapsulant ethylene vinyl acetate copolymer (EVA) in crystalline silicon photovoltaic modules: a review, Renew. Sustain. Energy Rev. 81 (2018) 2299–2317.
[32] W. Oh, S. Bae, S. Kim, N. Park, S.-I. Chan, H. Choi, H. Hwang, D. Kim, Analysis of degradation in 25-year-old field-aged crystalline silicon solar cells, Microelectron. Reliab. 100 (2019), 113392.
[33] O.K. Segbefia, N. Akhtar, T.O. Sætre, The effect of moisture ingress on titania antireflection coatings in field-aged photovoltaic modules, in: 2022 IEEE 49th Photovoltaics Specialists Conference (PVSC), IEEE, 2022, pp. 1237–1244.
[34] D.J. Colvin, N. Iqbal, J.H. Yerger, F. Li, A. Sinha, G. Vicnansky, G. Brummer, N. Zheng, E.J. Schneller, J. Barkaszi, Degradation of monocrystalline silicon photovoltaic modules from a 10-year-old Rooftop system in Florida, IEEE J. Photovoltaics 13 (2) (2023) 275–282.
[35] O.K. Segbefia, B.R. Paudyal, I. Burud, T.O. Sætre, Temperature Coefficients of Photovoltaic Modules under Partial Shading Conditions, 38th EU PVSEC, 2021, pp. 1180–1186.
[36] M. Köntges, A. Morlier, G. Eder, E. Fleiß, B. Kubicek, J. Lin, Ultraviolet Fluorescence as Assessment Tool for Photovoltaic Modules, IEEE J. Photovolt., 2020.
[37] A. Morlier, M. Siebert, I. Kunze, S. Blankemeyer, M. Köntges, Ultraviolet fluorescence of ethylene-vinyl acetate in photovoltaic modules as estimation tool for yellowing and power loss, in: 2018 IEEE 7th World Conference on Photovoltaic Energy Conversion (WCPEC)(A Joint Conference of 45th IEEE PVSC, 28th PVSEC & 34th EU PVSEC), IEEE, 2018, pp. 1597–1602.
[38] W. Herrmann, G. Eder, B. Farnung, G. Friesen, M. Köntges, B. Kubicek, O. Kunz, H. Liu, D. Parlevliet, I. Tsanakas, Qualification of Photovoltaic (Pv) Power Plants Using Mobile Test Equipment, 2021. IEA-PVPS T13-24: 2021.
[39] R. Meena, S. Kumar, R. Gupta, Comparative investigation and analysis of delaminated and discolored encapsulant degradation in crystalline silicon photovoltaic modules, Sol. Energy 203 (2020) 114–122.
[40] O.K. Segbefia, A.G. Imenes, I. Burud, T.O. Sætre, Temperature profiles of field-aged multicrystalline silicon photovoltaic modules affected by microcracks, in: 2021 IEEE 48th Photovoltaic Specialists Conference (PVSC), IEEE, 2021, pp. 1–6.
[41] E. Skoplaki, J.A. Palyvos, On the temperature dependence of photovoltaic module electrical performance: a review of efficiency/power correlations, Sol. Energy 83 (2009) 614–624.
[42] D.L. King, J.A. Kratochvil, W.E. Boyson, Temperature coefficients for PV modules and arrays: measurement methods, difficulties, and results, in: Conference Record of the Twenty Sixth IEEE Photovoltaic Specialists Conference-1997, IEEE, 1997, pp. 1183–1186.
[43] M.A. Green, General temperature dependence of solar cell performance and implications for device modelling, Prog. Photovoltaics Res. Appl. 11 (2003) 333–340.
[44] G. Segev, H. Dotan, D.S. Ellis, Y. Piekner, D. Klotz, J.W. Beeman, J.K. Cooper, D. A. Grave, I.D. Sharp, A. Rothschild, The spatial collection efficiency of charge carriers in photovoltaic and photoelectrochemical cells, Joule 2 (2018) 210–224.
[45] G.A. Landis, Review of solar cell temperature coefficients for space, in: XIII Space Photovoltaic Research and Technology Conference, SPRAT XIII, 1994, p. 385.
[46] S. Hoffmann, M. Koehl, Effect of humidity and temperature on the potential-induced degradation, Progress in Photovoltaics 22 (2014) 173–179.
[47] J.A. Tsanakas, L. Ha, C. Buerhop, Faults and infrared thermographic diagnosis in operating c-Si photovoltaic modules: a review of research and future challenges, Renew. Sustain. Energy Rev. 62 (2016) 695–709.
[48] S. Kajari-Schršder, I. Kunze, M. Kšntges, Criticality of cracks in PV modules, Energy Proc. 27 (2012) 658–663.
[49] C. Buerhop, D. Schlegel, M. Niess, C. Vodermayer, R. Weißmann, C. Brabec, Reliability of IR-imaging of PV-plants under operating conditions, Sol. Energy Mater. Sol. Cells 107 (2012) 154–164.
[50] W. Chen, Y. Liu, L. Yang, J. Wu, Q. Chen, Y. Zhao, Y. Wang, X. Du, Difference in anisotropic etching characteristics of alkaline and copper based acid solutions for single-crystalline Si, Sci. Rep. 8 (2018) 1–8.
[51] J. Li, Y.-C. Shen, P. Hacke, M. Kempe, Electrochemical mechanisms of leakage-current-enhanced delamination and corrosion in Si photovoltaic modules, Sol. Energy Mater. Sol. Cells 188 (2018) 273–279.
[52] J. Bauer, V. Naumann, S. Großer, C. Hagendorf, M. Schütze, O. Breitenstein, On the mechanism of potential-induced degradation in crystalline silicon solar cells, Phys. Status Solidi Rapid Res. Lett. 6 (2012) 331–333.
[53] B. Smets, T. Lommen, The leaching of sodium containing glasses: ion exchange or diffusion of molecular water? J. Phys. Colloq. 43 (1982). C9-649-C649-652.
[54] R. Wiesinger, S. Schnöller, H. Hutter, M. Schreiner, C. Kleber, About the formation of basic silver carbonate on silver surfaces–An in situ IRRAS study, Open Corrosion J. 2 (2009).
[55] S. Meyer, S. Timmel, M. Gläser, U. Braun, V. Wachtendorf, C. Hagendorf, Polymer foil additives trigger the formation of snail trails in photovoltaic modules, Sol. Energy Mater. Sol. Cells 130 (2014) 64–70.
[56] H.-J. Freund, M.W. Roberts, Surface chemistry of carbon dioxide, Surf. Sci. Rep. 25 (1996) 225–273.
[57] C. Oh, A. Kim, J. Kim, J. Bang, J. Ha, W.-S. Hong, Bonding copper ribbons on crystalline photovoltaic modules using various lead-free solders, J. Mater. Sci. Mater. Electron. 26 (2015) 9721–9726.
[58] P. Chaturvedi, B. Hoex, T.M. Walsh, Broken metal fingers in silicon wafer solar cells and PV modules, Sol. Energy Mater. Sol. Cells 108 (2013) 78–81.
[59] C.M. Oertel, S.P. Baker, A. Niklasson, L.-G. Johansson, J.-E. Svensson, Acetic acid vapor corrosion of lead–tin alloys containing 3.4 and 15% tin, J. Electrochem. Soc. 156 (2009) C414.
[60] S. Msallamova, M. Kouril, K.C. Strachotova, J. Stoulil, K. Popova, P. Dvorakova, M. Lhotka, Protection of lead in an environment containing acetic acid vapour by using adsorbents and their characterization, Heritage Science 7 (2019) 1–9.
[61] A. Niklasson, L.-G. Johansson, J.-E. Svensson, Influence of acetic acid vapor on the atmospheric corrosion of lead, J. Electrochem. Soc. 152 (2005) B519.